Enabling plasmon-assisted ammonia synthesis: from mechanistic insights to catalyst design

Wen-Qian Li,[a] Miao Xu,[b] Gang Chen,[cd] Xiaoping Chen, [ID] *[cd] Jie-Sheng Chen [ID] [a] and Tian-Nan Ye [ID] *[a]

Ammonia is an important component in the manufacture of fertilizers and various chemicals, and its production mainly relies on the energy-intensive Haber–Bosch process. To overcome this, there has been growing interest in using photocatalysis as an alternative approach for ammonia synthesis under ambient conditions. Plasmonic nanomaterials have been considered to be particularly promising due to their localized surface plasmon resonance (LSPR) effects that combine the advantages of photochemical and thermal properties in one system. This review introduces the fundamental principles of LSPR effects, including hot carrier injection, photoheating and near-field enhancement. It then undertakes a comprehensive analysis of the current state-of-the-art catalysts for plasmon-driven photocatalytic ammonia synthesis. Finally, it proposes a brief outlook on the strategies for the design of plasmonic photocatalysts, advances in *in situ* characterization and theoretical simulations, standardization of the reaction conditions and detection technologies for ammonia production.

1. Introduction

Ammonia, as one of the most important feedstocks, has been widely used for the production of fertilizers and various chemicals.[1–3] In 1913, the Haber–Bosch process was invented for the industrial production of ammonia. Since then, much effort has been devoted to the development of catalysts for ammonia synthesis. Adding electron promoters, such as potassium (K), potassium oxide (K_2O), potassium hydroxide (KOH), and others, can enhance the catalytic activity for ammonia production. Additionally, structure promoters like aluminium oxide (Al_2O_3), manganese oxide (MnO), zirconium oxide (ZrO_2), and chromic oxide (Cr_2O_3) can further improve the catalytic performance. Optimization of these factors can lead to more efficient and selective ammonia synthesis. However, the ammonia synthesis over iron-based catalysts often requires high temperatures (400–500 °C) and pressures (10–30 MPa) to obtain a high ammonia yield. In contrast, ruthenium-based catalysts have received significant attention due to their ability to facilitate ammonia production under relatively mild reaction conditions compared to iron-based catalysts. For instance, a graphite-supported ruthenium catalyst has been industrially applied in KBR's advanced ammonia synthesis process (KAAP).[4] Despite its high efficiency, the use of ruthenium metal on a large scale has been hindered by its scarcity and high cost, as well as the inevitable methanation of carbon-based supports. Moreover, the traditional thermochemical process accounts for 1–2% of the world's total energy consumption and consumes *ca.* 50% of the global hydrogen production, which is largely based on fossil resources.[5] As a result, the production of each ton of ammonia is associated with the emission of approximately 2 tons of carbon dioxide, representing around 3% of the total greenhouse gas emissions.[6] Therefore, there is a pressing need to explore alternative and sustainable strategies for ammonia synthesis.

The pursuit of such sustainable strategies has catalysed the emergence of the "green ammonia" concept, which aims to fully decarbonize the ammonia synthesis process by leveraging renewable energy sources.[7,8] A key step towards this goal is to replace natural gas-derived H_2 with water as the hydrogen source to produce NH_3 ($2N_2 + 6H_2O \rightarrow 4NH_3 + 3O_2$).[9,10] Photocatalysis offers a promising solution for this purpose, as it enables ammonia synthesis at lower temperatures and pressures while utilizing renewable energy sources. In the early 1970s, Schrauzer and Guth reported the first instance of photocatalytic ammonia synthesis. Since then, extensive research has been devoted to developing efficient catalysts for photocatalytic ammonia synthesis (Fig. 1).[11] During the photocatalysis process, exposure to solar light causes the absorption of light energy, leading to a separation of the electron–hole pairs. Electrons are excited into the conduction band (CB) of the semiconductor for

[a]Frontiers Science Center for Transformative Molecules, School of Chemistry and Chemical Engineering, Shanghai Jiao Tong University, Shanghai 200240, China. E-mail: ytn2011@sjtu.edu.cn

[b]State Key Laboratory of Space Power-Sources Technology, Shanghai Institute of Space Power-Sources, Shanghai 200245, China

[c]Institute of Energy Research, Jiangxi Academy of Sciences, Nanchang 330096, China. E-mail: cxpjxskxy@126.com

[d]Jiangxi Carbon Neutralization Research Centre, Jiangxi Academy of Sciences, Nanchang 330096, China
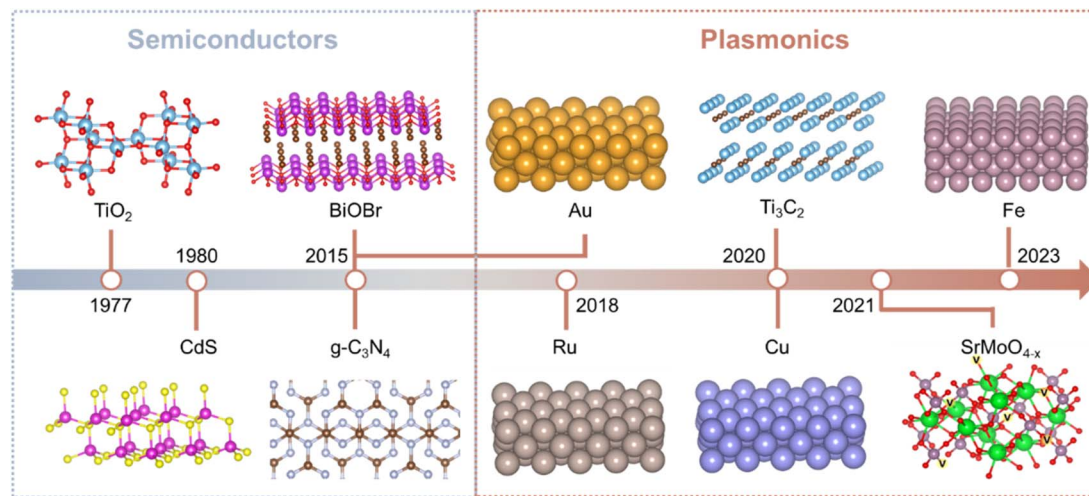
Fig. 1 The historical progression of typical photocatalysts for ammonia synthesis.

N_2 reduction. Meanwhile, holes in the valence band (VB) facilitate the oxidation of H_2O to O_2 as well as the release of protons that combine with N atoms to form NH_3. To date, various semiconductor materials have been explored as photocatalysts for ammonia synthesis, including oxides,[12] sulfides,[13] bismuth oxyhalides,[9] carbonaceous materials[14] and so on. Recently, it was reported that defective pyrochlore $K_2Ta_2O_{6-x}$, loaded with Ru and characterized by a very low work function, facilitated efficient photocatalytic ammonia synthesis.[12] The effectiveness of this process is primarily due to a synergistic effect: efficient charge separation, paired with spontaneous electron transfer, which is enhanced by the presence of oxygen defects. In addition to metal oxides, metal sulfides have attracted attention owing to their ability to absorb visible light.[15] CdS was the first metal sulfide applied in photocatalytic ammonia synthesis,

followed by other metal sulfides such as FeMoS chalcogels and Fe-decorated 2D-MoS$_2$.[13,16] However, the low physicochemical stability of metal sulfides hinders their further development. In recent years, two-dimensional materials such as bismuth oxyhalides,[9] g-C$_3$N$_4$[14] and LDHs[17] have gained attention in photocatalytic ammonia synthesis due to their quick electron transfer and large specific surface area. Bismuth oxyhalides have an internal electric field, which can promote carrier separation, while g-C$_3$N$_4$ was the first organic material used for photocatalytic ammonia synthesis, opening up research on organic photocatalysts. LDHs have a facilely controllable metal cation composition, allowing for the easy construction of defect and regulation of the band structure. Despite such encouraging progress, most photocatalysts continue to face challenges in achieving efficient photocatalytic N_2 reduction (Fig. 2): (1)
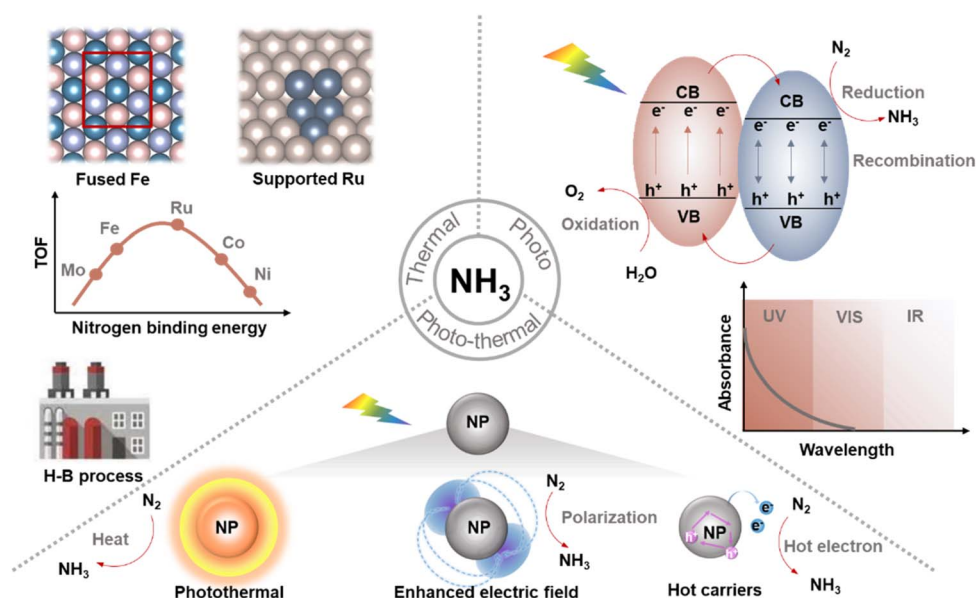

Fig. 2 The history, innovations, and challenges of ammonia synthesis through thermochemical, photochemical, and photo-thermal processes.

inherent limitations of semiconductor photocatalysts in light harvesting and utilization; (2) the undesirable recombination of excited electron–hole pairs that decreases the catalytic efficiency; (3) inadequate active sites and sluggish reaction kinetics that hamper N_2 activation. Consequently, there is still a pressing need to broaden the scope of light-driven catalysis and enhance the efficiency of photocatalysts.

Plasmonic photocatalysis has emerged as a promising technique for driving various chemical reactions, including CO_2 reduction, water-splitting reactions, and organic compound transformations.[18–24] Compared to semiconductors, plasmonic nanomaterials can absorb light across a wider range of the solar spectrum, from ultraviolet spectrum (UV) to near-infrared spectrum (NIR). The localized surface plasmon resonance (LSPR) of plasmonic nanomaterials, such as Ag, Au, and Cu nanoparticles, contributes to the high efficiency of plasmonic photocatalysis.[25] On the one hand, the photo-induced electrons originating from plasmonic materials are transferred to the antibonding π orbital of N_2 to activate N_2. On the other hand, the photoheating effect can reduce the energy barrier for N_2 activation. In addition, the enhanced electric field derived from plasmonic materials can polarize the $N\equiv N$ bond, facilitating the N_2 dissociation (Fig. 2).[26] By utilizing solar energy, this photo-thermal catalysis combines photochemical and thermo-chemical processes, leading to exceptional catalytic activity under mild conditions. To date, only a few reviews have reported on plasmon-enhanced ammonia synthesis. However, the focus of those reviews was on the state-of-the-art plasmonic catalysts rather than on the promotion mechanism for the ammonia synthesis process.[27–29] In this review, we aim to provide a systematic summary of the fundamental principles of LSPR and to clearly demonstrate the promotion effects of LSPR in plasmonic-based ammonia synthesis. Herein, we will present the basics of LSPR and its underlying mechanisms, followed by a detailed examination of strategies for ammonia synthesis via plasmonic photocatalysis. Ultimately, we will conclude with a brief outlook on future directions.

2. LSPR effect promoted catalytic process

Upon irradiation with resonant light, plasmonic nanostructures exhibit Localized Surface Plasmon Resonance (LSPR),
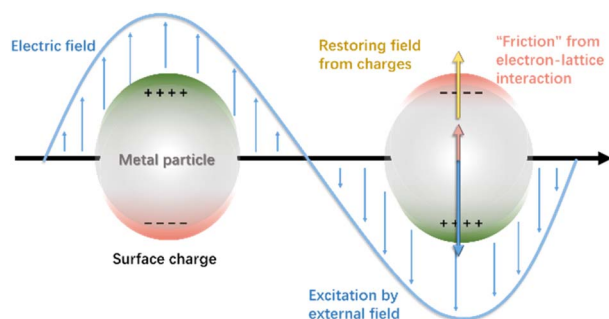

Fig. 3 Depiction of the dynamics of an excited plasmonic nano-particle (NP).

a collective oscillation of conduction electrons (Fig. 3).[30] The resonance condition is achieved when the photon frequency matches with the frequency of the free electrons oscillating against the restoring force of the nuclei. The decay of this coherent oscillation channels photon energy into three primary pathways that can enhance catalytic processes: the generation of energetic electron–hole pairs (hot carriers), local heating (photothermal effect), and the generation of a local electromagnetic field (near-field enhancement). These mechanisms can operate concurrently, and their relative contributions are governed by the material's electronic structure, nanostructure geometry, and the reaction environment. This section details these fundamental mechanisms and provides a framework for their experimental discrimination, which is critical for the rational design of plasmonic catalysts.

2.1. Hot carrier generation

Plasmon decay can occur through radiative or non-radiative processes, with the latter generating hot electron–hole pairs within the plasmonic nanostructure.[31,32] The generation of charge carriers may occur via intraband s-to-s excitation or interband d-to-s excitation, with the latter being dominant when energetically accessible.[32] For noble metals like Ag, visible light cannot induce interband excitations due to their d-bands being far below the Fermi level. In contrast, Au and Cu can be excited by visible light because their d-bands are closer to the Fermi level. For non-noble metals, incomplete d-states intersect the Fermi level, allowing interband transitions across the visible range.[33]

However, charge carriers generated from plasmon decay have very short lifetimes of 1–100 fs, much shorter than those in semiconductors and molecular photocatalysts.[33] To utilize these short-lived carriers in catalysis, they must be either extracted or leveraged.[34] Two mechanisms for charge transfer have been identified: indirect charge transfer, where energetic carriers are generated in the plasmonic metal and later transferred to an adsorbate's unoccupied molecular orbital or a semiconductor's conduction band, and direct charge transfer, which involves the immediate excitation of charge carriers from the metal to hybridized metal–adsorbate interfacial states during plasmon decay.

To harness the full potential of hot carriers generated by plasmonic materials, several approaches have been employed in the design of plasmon-based catalysts. The first strategy involves constructing a hybrid structure of plasmon and semiconductor particles. In this design, plasmonic nanoparticles act as electron traps, transferring hot electrons to the conduction band of the semiconductor through a Schottky barrier (Fig. 4a).[35] However, only a limited number of energetic electrons can be successfully transferred due to the high Schottky barrier (A Schottky barrier is a metal–semiconductor junction that exhibits rectifying behaviour, meaning it allows current to flow more easily in one direction than the other.) (Fig. 4b). To overcome this barrier, it is essential to establish a suitable interface between the plasmonic nanoparticles and the semiconductors. The second strategy involves combining two
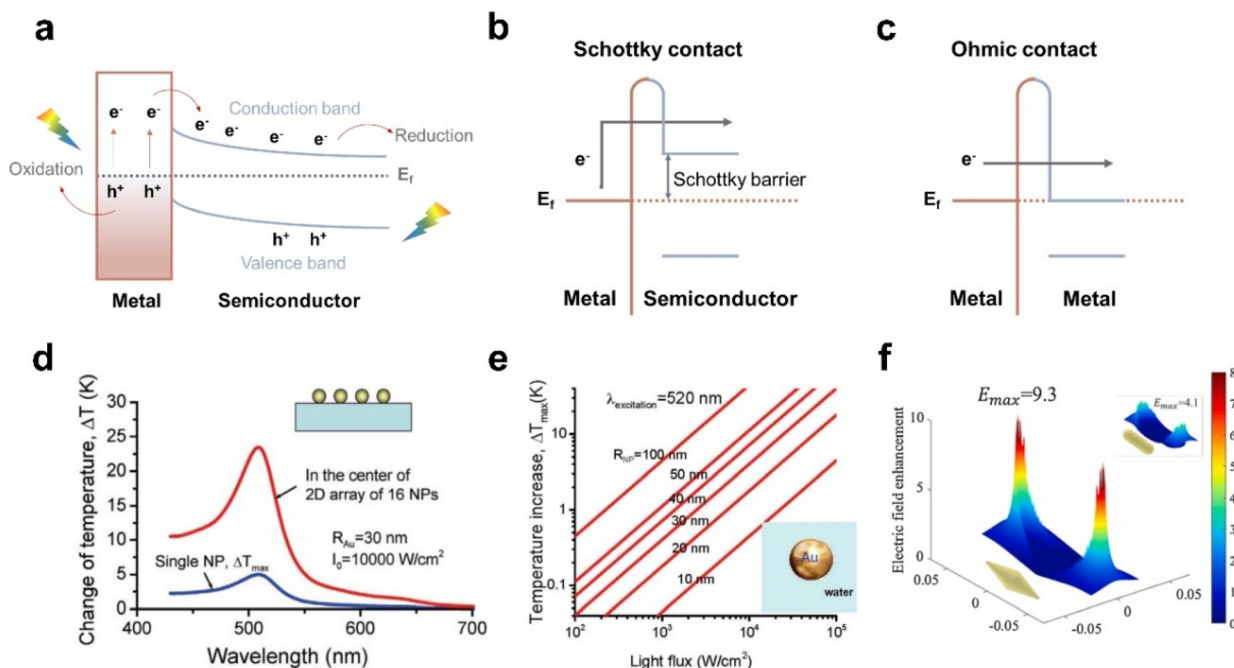
Fig. 4 (a) The scheme of photocatalytic mechanism over a metal–semiconductor system. (b) The scheme of Schottky contact. (c) The scheme of ohmic contact. (d) Calculated temperature increase in the centre of a square array of 16 NPs. (e) Calculated temperature increase on the surface of a single Au NP as a function of illumination power at the plasmon resonance. Reproduced with permission[43]. Copyright 2007, Elsevier. (f) Electric field enhancement of the Au nano-bipyramid and Au nanorod. Reproduced with permission[44]. Copyright 2007, Elsevier.

different metals (Fig. 4c). In this approach, plasmonic metal generates hot electrons that are transferred to the active transition metal, which provides active sites for N_2 adsorption and activation. This approach is closer to an ohmic contact (an ohmic contact is a metal–semiconductor junction that exhibits linear or Ohm's law behaviour, meaning it allows current flow equally well in both directions), which requires a lower energy barrier for electron transfer.[35]

2.2. Photothermal effect

Upon excitation of the plasmon, the hot electrons and holes are generated within 100 fs upon plasmon decay. With longer relaxation times, hot carriers decay and convert the stored energy into heat. The resulting heat can be released into the surroundings through phonon–phonon scattering, leading to a locally elevated temperature.[36–38] The heating energy produced by the LSPR effect in plasmonic materials has shown significant potential in various scientific and technological applications, such as photo-thermal therapy for cancer, biochemical sensing, and solar steam generation.[39–42] In addition, the heat generated by photons facilitates energy transfer from plasmonic materials to surface adsorbates, driving chemical reactions. It is noted that the heat generated by photons can only elevate the local temperature but has no impact on the modulation of the selectivity of the reactions.

The photoheating effect is minimal when applied to a single metal nanoparticle.[45] However, as the number of nanoparticles (NPs) increased, the photoheating effect can significantly enhance due to the accumulative effect.[43] Fig. 4d shows the calculated temperature increase in the centre of a square array

of 16 NPs. It is evident that the more the number of NPs, the stronger the temperature increase observed in the system. The photoheating effect is also highly dependent on the particle size of plasmonic metals. As shown in Fig. 4e, the NP with a larger radius shows a stronger temperature increase.[43] Photoheating is a ubiquitous phenomenon in plasmonic systems, significantly enhancing the dynamic process and increasing the yield of the product. The use of temperature-sensitive photocatalysts offers promising opportunities to harness the photoheating effect.

2.3. Optical near-field enhancement

The generation of a local electric field is a crucial property of LSPR in plasmonic materials. At resonance, the collective oscillation of the electron cloud causes near-field enhancement, resulting in a localized increase in the density of photonic states. The near field is highly localized and limited to only a few nanometres around the surface of the plasmonic metal. When reactant molecules are adsorbed on the active sites of plasmonic photocatalysts under irradiation, metal–adsorbate complexes are generated. The plasmonic components create a local field around the complex, facilitating the polarization of adsorbates and efficient activation of reactants. This near-field enhancement enables the direct optical transition of reactants and allows for plasmonic resonance to overlap spectrally with absorption bands, thereby enhancing optical excitation.

2.4. Experimental methods for the reaction mechanisms

Deconvoluting the contributions of hot carriers, photothermal effects, and near-field effects is a central challenge since they

often coexist. Fig. 5 provides a concise visual guide to the experimental methodologies used to distinguish between these effects in plasmonic photocatalysis.

The photocatalytic rate's dependence on light intensity is a powerful analytical tool for understanding the reaction mechanisms. Four kinetic categories related to the light intensity (I) and photocatalytic reaction rate have been documented: sublinear (rates $\propto I^n$, $n <1$), linear (rates $\propto I$), superlinear (rates $\propto I^n$, $n >1$), and exponential (rates $\propto e^{f(I)}$). Sublinear dependence is typical in non-plasmonic semiconductors where charge carrier recombination is dominant. A linear reaction rate with light intensity is a hallmark of electron-driven processes, commonly reported in plasmonic reactions (Fig. 5a).[46] Superlinear behavior may also suggest hot carrier-driven transformations, where multiple excitations of vibrational modes by hot electrons lead to enhanced reactions. Conversely, if photothermal effects dominate, the reaction shows Arrhenius-type behavior, exhibiting exponential dependence on light intensity.

The dependence of reaction rates on photon wavelength can further indicate hot carrier-driven processes (Fig. 5b). A correlation between the absorption spectrum of the plasmonic photocatalyst and wavelength-dependent reaction rates supports electron-driven photochemical transformations.[47] Transient absorption spectroscopy (TAS) is effective for studying electron transfer dynamics (Fig. 5c).[48] Rapid electron transfers occur within hundreds of femtoseconds, while the transient signal's decay lasts thousands of nanoseconds, indicating effective charge carrier separation and reduced recombination. Other techniques, like photoluminescence analysis and photovoltage measurements, can also identify hot electron transfer and charge separation.

For photothermal effects, direct temperature measurements at active sites are critical (Fig. 5d).[49] Recent advancements in nanoscale thermometry include non-luminescence methods, like scanning thermal microscopy, which achieves a spatial resolution of 10 nm with 10–50 mK precision, and luminescence methods such as thermoreflectance and optical interferometry. Thermoreflectance utilizes the correlation between a material's refractive index and temperature, creating temperature profiles with high resolution. Additionally, tip-
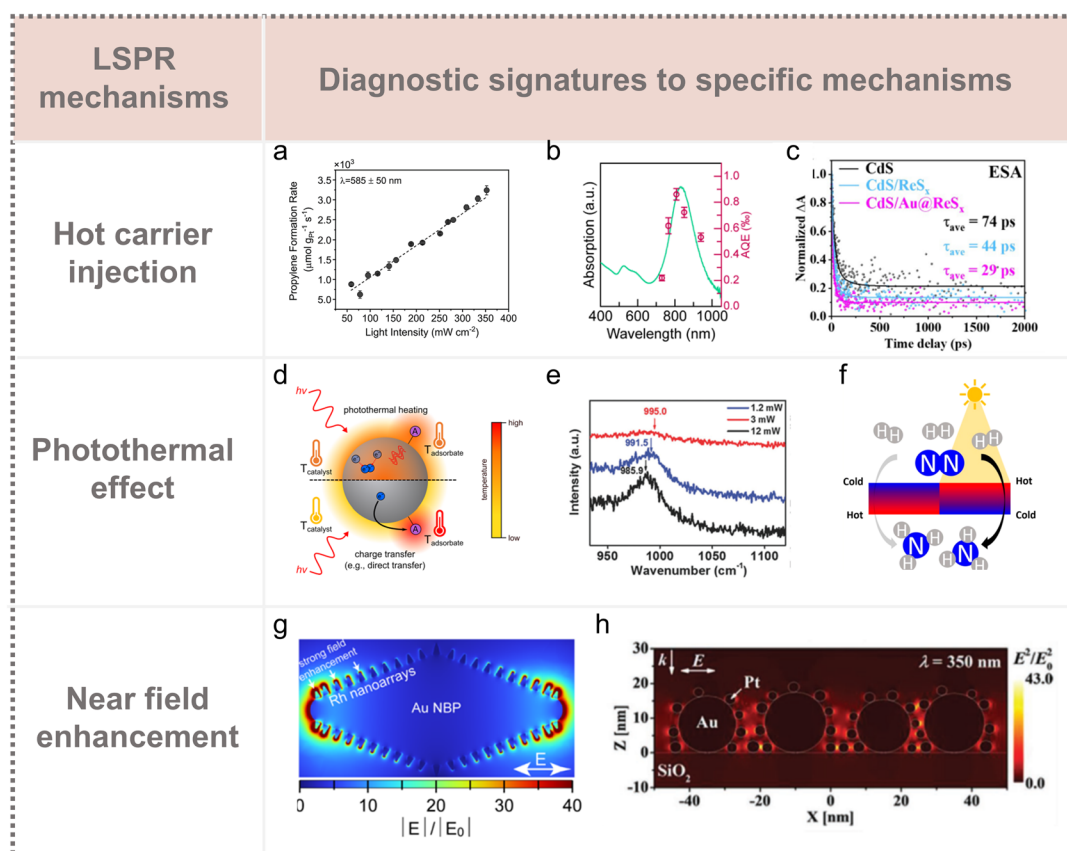

Fig. 5 (a) Power-dependent study of CuPt$_{SA}$ (246 : 1) disentangling photothermal and nonthermal effects on plasmonic propane dehydrogenation at 460 °C. Reproduced with permission[46]. Copyright 2025, American Chemical Society. (b) Absorption and AQE action spectra of the Au NBP/Rh SSs. Reproduced with permission[47]. Copyright 2024, American Chemical Society. (c) The corresponding fs-TAS decay curves at 500 nm for various samples in the lactic acid solution. Reproduced with permission[48]. Copyright 2025, American Chemical Society. (d) Energy transfer pathways for photomediated chemistry on a plasmonic metal nanoparticle catalyst. Reproduced with permission[49]. Copyright 2024, American Chemical Society. (e) Raman frequency dependence for Nb−O stretching vibrations. Reproduced with permission[50]. Copyright 2017, Wiley-VCH. (f) Cs−Ru/MgO for photocatalytic ammonia synthesis. Reproduced with permission[51]. Copyright 2019, The American Chemical Society. (g) FDTD analysis of Au NBPs. Reproduced with permission[47]. Copyright 2024, American Chemical Society. (h) FDTD simulation of electric field intensity distribution in the Pt−Au/SiO$_2$ system. Reproduced with permission[52]. Copyright 2018, American Chemical Society.

enhanced Raman spectroscopy (TERS) can map local temperatures at the nanometer scale by calculating the ratio of anti-Stokes to Stokes Raman signal intensities. For example, Ozin *et al.* investigated a Pd/Nb_2O_5 catalyst for CO_2 photocatalytic reduction, using Stokes and anti-Stokes Raman bands to determine the local catalyst temperature (Fig. 5e).[50] Their findings suggested that Pd NPs act as photothermal "nano-heaters", effectively raising local temperatures to enhance CO_2 hydrogenation. Controlled experiments are also crucial for identifying photothermal effects. For example, Li *et al.* demonstrated that using a black photothermal material could completely suppress hot electron transfer, converting all light into heat (Fig. 5f).[51]

To identify local near-field-driven plasmonic photocatalysis mechanisms, various methods have been employed. The finite difference time domain (FDTD) method is a widely used numerical tool for full-wave electromagnetic field analysis. In plasmonic photocatalysis, FDTD simulations can evaluate the interaction between light and nanoparticles, providing insights into optimizing systems through near-field distribution and intensity enhancement.[46] Recently, Yang *et al.* used FDTD to simulate electric field enhancement from Au nano-bipyramids (Fig. 5g), analyzing physical parameters such as the aspect ratio and excitation wavelength.[47] Additionally, constructing bimetallic plasmonic photocatalysts can enhance plasmonic coupling between materials, leading to significant electric fields and efficient electron transfer (Fig. 5h).[52]

3. LSPR enhanced ammonia synthesis

3.1. Hot carrier enhanced ammonia synthesis

3.1.1. Oxygen vacancy site promoted N_2 activation. A central challenge in harnessing the LSPR effect is the efficient extraction and utilization of generated hot carriers before their intrinsic relaxation. While plasmonic nanostructures act as potent nano-antennas for light absorption and hot carrier generation, their intrinsic recombination is rapid. Thus, the strategic design of electron acceptors interfaced with the plasmonic metal is critical to channel these energetic electrons toward targeted redox reactions, such as nitrogen reduction.

A highly effective strategy involves the introduction of defects, particularly vacancies, in semiconductor supports or co-catalysts. These vacancies function as effective electron traps, capturing plasmon-derived hot electrons and thereby mitigating charge recombination. Concurrently, they often serve as active sites for molecular adsorption and activation.[9,56,57] For instance, oxygen vacancies in TiO_2 have been extensively studied in this field. A representative system involves Au nanoparticles anchored on TiO_2 nanosheets with sufficient oxygen vacancies, which were synthesized by the solvothermal method.[53] In this architecture, the Au NPs act as optical antennas, generating hot electrons upon irradiation, which are subsequently transferred to the TiO_2 conduction band and ultimately captured by the oxygen vacancies. These vacancy-trapped electrons then drive the activation and reduction of adsorbed N_2 molecules (Fig. 6a). However, the oxygen vacancies are generated by the solvothermal method, a process that creates defects in the bulk phase. These defects may act as

carrier traps, leading to the recombination of photogenerated electron–hole pairs, significantly reducing the overall quantum efficiency. Simultaneously, bulk defects are located within the material's interior, limiting access to reactant molecules and thereby reducing the density of active sites. In contrast, surface defects circumvent these limitations, effectively trapping photogenerated electrons to suppress bulk recombination while enabling rapid transfer to surface adsorbates. This direct pathway enhances interfacial charge transfer and improves surface reaction kinetics. This principle was demonstrated in a system where surface oxygen vacancies were precisely created on plasmonic TiO_2/Au nanorods *via* atomic layer deposition.[54] The confinement of vacancies to the surface region preserved the bulk properties of TiO_2 and provided abundant, accessible active sites for N_2 activation, leading to a significantly enhanced NH_3 yield compared to the system with bulk defects (Fig. 6b).

Beyond optimizing material-based electron acceptors, the reaction microenvironment at the solid–liquid interface can be strategically engineered to enhance plasmon-mediated N_2 reduction further. Introducing alkali and alkaline earth metal (AM) cations (*e.g.*, K^+, Na^+, *etc.*) into the reaction system has proven to significantly boost catalytic activity (Fig. 6c–e), building on the foundation provided by optimized electron acceptors like oxygen vacancies.[55] The promotional effect of these cations is primarily due to the formation of a strong local electric field at the catalyst–solution interface, rather than direct involvement in the charge trapping process. It is proposed that this cation-induced electric field effectively stabilizes key intermediates generated during the N_2 reduction process, subsequently lowering the activation energy barrier for the rate-determining step.[49] However, this mechanism remains speculative, as direct evidence for the presence and role of such a field is lacking. In a related study on electrocatalytic CO_2 reduction, Chen *et al.* developed a microkinetic model incorporating electric field effects from *ab initio* calculations. Their work demonstrated that the field from solvated cations in the double layer, along with their image charges on the metal surface, can significantly stabilize critical intermediates like $*CO_2$.[58] These findings support the notion that cations can indeed influence key intermediates through local field effects. To gain deeper insights into the cation-induced electric field mechanism, future investigations will require more experimental evidence, such as advanced *in situ* FT-IR and *in situ* XPS measurements capable of probing the interaction between the electric field and reaction intermediates in real-time.

The strategy of optimizing electron acceptors can be extended beyond TiO_2 to other reducible oxides, such as ceria (CeO_2), which features a reversible Ce^{4+}/Ce^{3+} redox couple associated with oxygen vacancy formation. A noteworthy example is the site-selective growth of Au nanorods capped with crystalline CeO_2 at their ends.[50] This unique spatial configuration, with oxygen vacancies localized in the ceria domains, facilitates improved charge separation. Plasmon-induced hot electrons generated in the Au nanorods are efficiently transferred to the oxygen vacancy sites of CeO_2 for N_2 activation, while the hot holes are scavenged by a sacrificial agent. As a result, this system demonstrates enhanced N_2 fixation activity
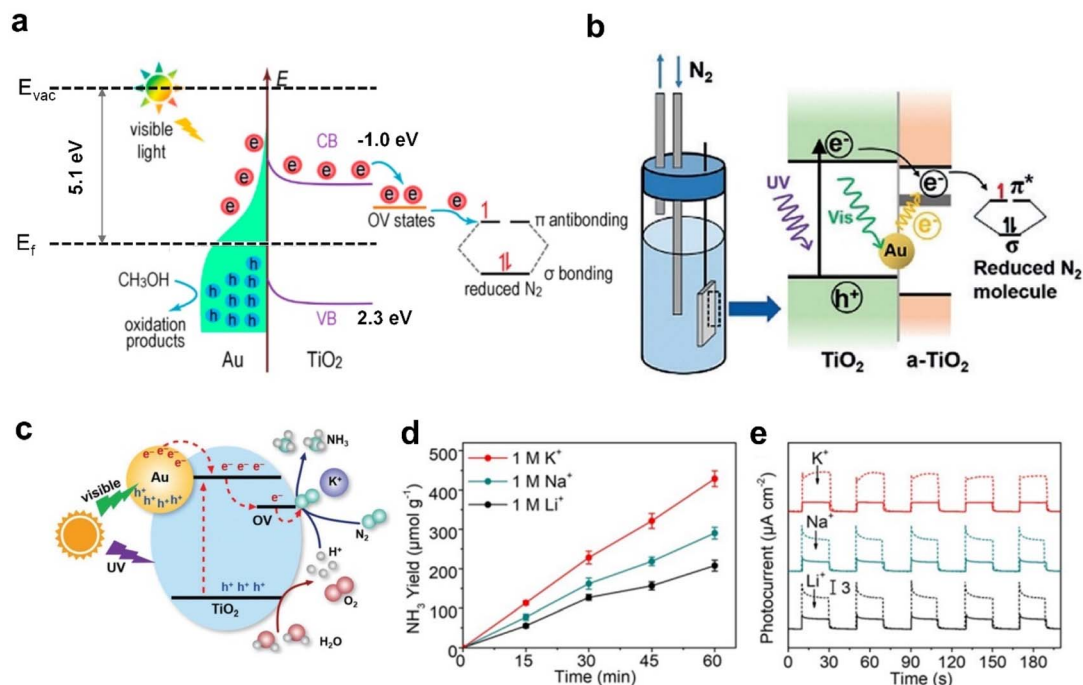
Fig. 6 (a) Schematic illustration of the hot-electron generation, injection and N_2 reduction over Au/TiO_2 with oxygen vacancies. Reproduced with permission.[53] Copyright 2018, American Chemical Society. (b) An illustration of the synergistic effect of surface oxygen vacancies and plasmonic Au NPs for ammonia synthesis. Reproduced with permission.[54] Copyright 2018, Wiley-VCH. (c) Schematic illustration of the plasmonic photocatalytic ammonia synthesis. (d) NH_3 yield on Au/TiO_2 with different alkali metal cations. (e) Cathodic photocurrent on Au/TiO_2 with different alkali metal cations. Reproduced with permission.[55] Copyright 2019, The Royal Society of Chemistry.

under near-infrared illumination (Fig. 7a–c). Another interesting work reported that abundant surface vacancies of CeO_2 can effectively stabilize the individual Ru atoms.[60] Under illumination, CeO_2 generates electron–hole pairs, with electron captures by the Ru sites. The electron-rich Ru site can effectively activate N_2 molecules, which reduce the energy barrier of the rate-limiting step, thereby enhancing the ammonia synthesis performance.

The scope of plasmonic materials has expanded to include certain inorganic compounds beyond metal nanoparticles, such

Fig. 7 (a) Schematic illustration of the synthesis of Au/end CeO_2. (b) Mechanism of N_2 photofixation for Au/end-CeO_2. (c) Comparison of the hot carrier separation behaviours of Au/end-CeO_2 with that of the core@shell nanostructure. Reproduced with permission.[59] Copyright 2019, American Chemical Society.

as $Ti_3C_2T_x$, MoO_3, and $SrMoO_4$. $Ti_3C_2T_x$ is a typical 2D MXene material,[61–64] which shows intrinsic LSPR in the visible to near-infrared range.[65,66] This LSPR behavior fundamentally arises from the material's unique electronic structure, which is directly reflected in its optical constants ($\tilde{n} = n + ik$). The high concentration of Drude-like free electrons inherent to the metallic Ti_3C_2 core results in a large negative real part of the dielectric function (ε_1) in the visible-NIR region,[67] which is essential for LSPR excitation. Additionally, significant optical absorption, characterized by a substantial extinction coefficient (k), leads to the observed strong LSPR peaks. The surface functional groups ($T_x = -O$, $-OH$, and $-F$) critically modulate these optical constants by acting as n-type dopants. By withdrawing the electron density from the titanium layers, these terminations effectively increase the free carrier concentration. This, in turn, alters the plasma frequency and directly tunes the values of n and k, thereby enabling precise engineering of the LSPR wavelength and intensity. Consequently, the ability to tailor the optical constants through composition and structure makes $Ti_3C_2T_x$ a highly versatile and rationally designable platform for plasmon-enhanced applications. Similar to the LSPR metals, single $Ti_3C_2T_x$ often shows inadequate charge carrier separation efficiency, limiting its usefulness in plasmonic photocatalysis. A promising approach to solve this dilemma involves creating vacancies to hinder carrier recombination. Hou et al. designed $Ti_3C_2T_x/TiO_2$ hybrid structures, in which $Ti_3C_2T_x$ serves as the plasmonic component, triggering the generation of hot electrons upon light absorption, while the oxygen vacancies in TiO_2 act as catalytically active sites for N_2
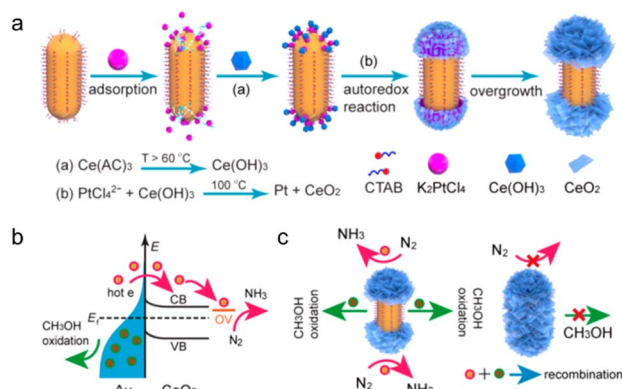
activation.[68] Such a hybrid structure (Fig. 8a) greatly enhances the efficiency of photocarriers, leading to excellent performance in photocatalytic ammonia synthesis.

In addition to MXenes, some non-stoichiometric oxides, such as MoO_{3-x} and $SrMoO_4$, also exhibit LSPR behaviour. For MoO_{3-x}, the LSPR is primarily driven by the introduction of oxygen vacancies. These vacancies act as intrinsic donors, generating a high concentration of free electrons by reducing Mo^{6+} to Mo^{5+} states. The collective oscillation of these vacancy-induced free carriers upon photoexcitation results in a strong, tunable LSPR absorption. Recently, a single MoO_{3-x} nanosheet with a high charge carrier density of 7.46×10^{20} cm^{-3} was reported to achieve the N_2 photofixation in pure water under visible to NIR plasmonic excitation. Abundant OVs and Mo^{5+} centres coexist in this "two-in-one" semiconductor, enabling the introduction of rich active sites and broad spectrum LSPR-induced hot electrons with a high reductive potential into one nanostructure (Fig. 8b).[69] Such a strategy endows the MoO_{3-x} nanosheet a high ammonia synthesis rate without the need for any other co-catalyst, providing a new route for the design and fabrication of plasmonic semiconductors.

Similarly, plasmonic $SrMoO_4$ can also be obtained by annealing $SrMoO_4$ in hydrogen, creating abundant oxygen vacancies with a high charge carrier density of $\sim 2.0 \times 10^{20}$ cm^{-3} and leading to add-on states close to the Fermi level (Fig. 8c).[70] Upon excitation, plasmonic hot electrons are transformed to the conduction band (Fig. 8d), allowing efficient harvesting of the visible and near-infrared light. These hot electrons are energetic enough to trigger the photocatalytic nitrogen reduction reaction. As a result, the plasmonic $SrMoO_4$ shows enhanced

photocatalytic nitrogen reduction performance under irradiation of visible and near-infrared light. These semiconductors enrich the category of plasmonic materials significantly, making it feasible to design plasmonic semiconductor photocatalysts for ammonia synthesis.

3.1.2. Nitrogen vacancy site promoted N_2 activation. Recently, nitrogen vacancies are reported to be effective for N_2 activation through a Mars–van Krevelen mechanism, in which the lattice N atom first reacts with dissociated H* step-by-step, releasing NH_3 and generating nitrogen vacancies. Then, N_2 molecules are subsequently activated at the defect sites and again react with H* to realize a stable catalytic cycle.[71,72] Guo et al. synthesized Au NPs-embedded hollow mesoporous carbon nitride spheres with abundant nitrogen vacancies, which served as active sites for trapping hot electrons generated on the plasmonic Au nanoparticles for N_2 activation (Fig. 9a).[73]

The shell thickness was another critical factor for the performance of photocatalysis as it determined the transport ability of the charge carriers while affecting the interplay of the total number of active sites on the surface and in the mesopores with ease of access. The highest productivity of ammonia was observed on carbon nitride with a shell thickness of 64 nm under visible-light illumination (Fig. 9b). The isotope labelling experiments showed that ammonia originates from nitrogen gas rather than carbon nitride (Fig. 9c). The reaction mechanism was further elucidated by DFT calculations. The nitrogen vacancies at the N site in HCNs-NV captured and held N_2 molecules through a di-nuclear end-on coordination mode. The charge density difference indicated that the localized electrons at the nitrogen vacancy sites cause a transfer of electrons to the
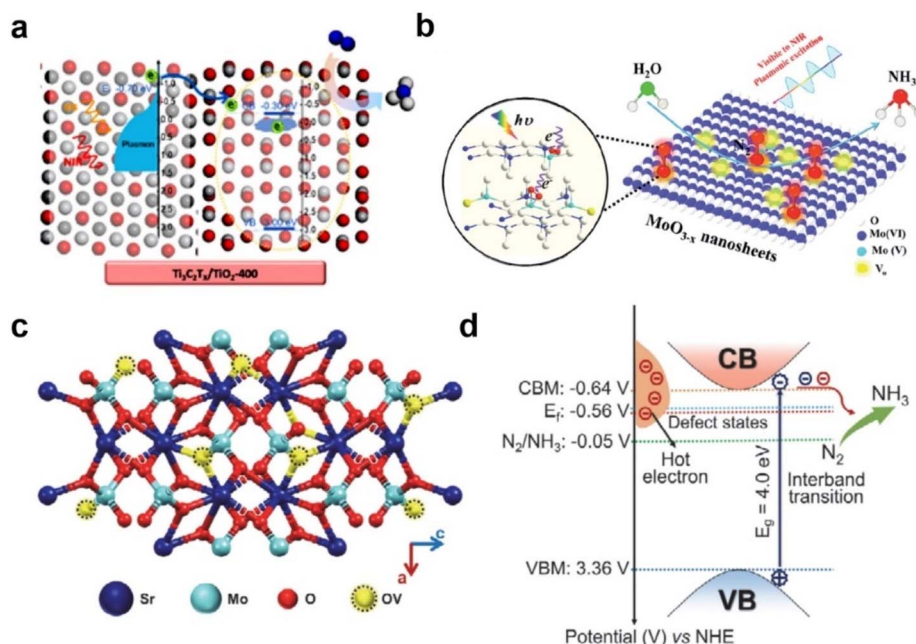

Fig. 8 (a) Schematic illustration of the electronic structures for $Ti_3C_2T_x/TiO_2$-400. Reproduced with permission.[68] Copyright 2020, Elsevier. (b) Schematic illustration of plasmonic photocatalytic N_2 fixation over MoO_{3-x}. Reproduced with permission.[69] Copyright 2020, The Royal Society of Chemistry. (c) The structure of $SrMoO_4$ with oxygen vacancies. (d) The mechanism for plasmonic photocatalytic nitrogen fixation over $SrMoO_4$ with oxygen vacancies. Reproduced with permission.[70] Copyright 2021, Elsevier.
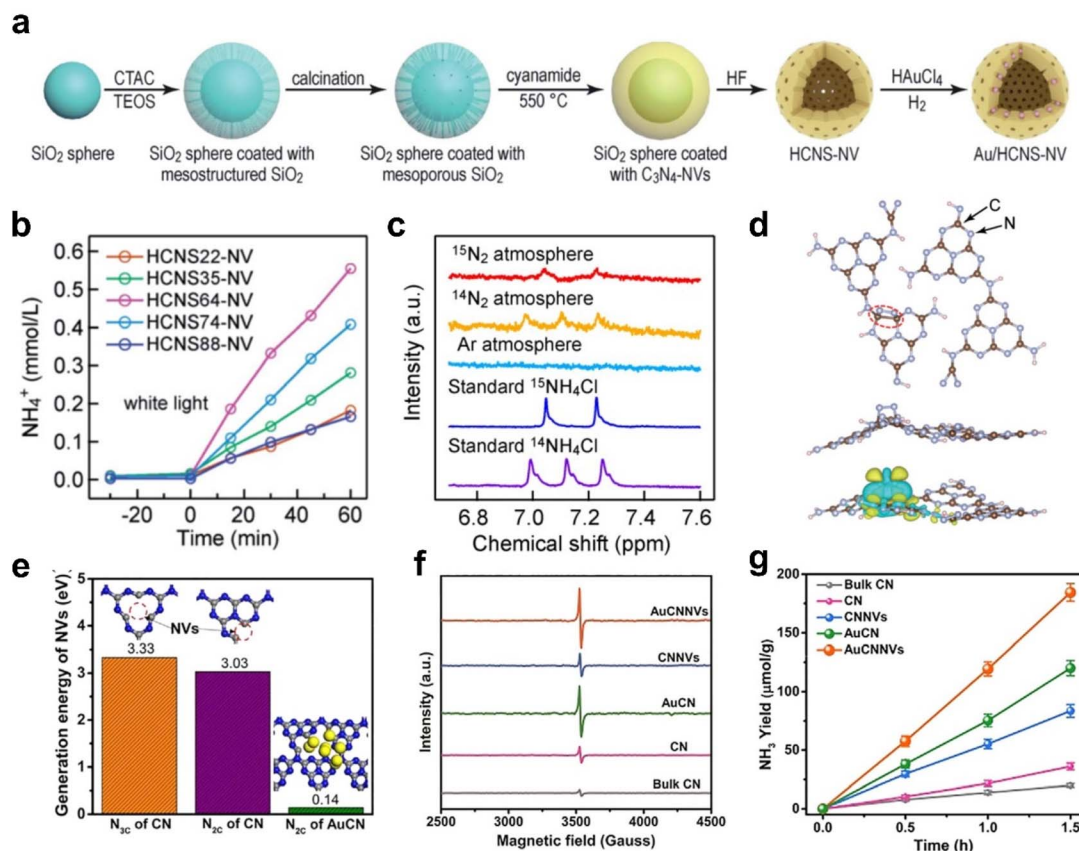
Fig. 9 (a) Synthesis of the Au/HCNS-NV. (b) NH_3 photocatalysis over HCNSx-NV. (c) ^1H NMR spectra of the reaction solution upon the photocatalytic N_2 fixation reaction for 2 h using Au/HCNS-NV as the catalyst in Ar, $^{14}N_2$ and $^{15}N_2$ atmospheres, respectively. (d) Adsorption configuration and charge density difference of N_2 adsorbed on the HCNS-NV. Reproduced with permission.[73] Copyright 2020, The Royal Society of Chemistry. (e) Nitrogen vacancy generation energies of different samples. (f) EPR spectra of different samples. (g) NH_3 yield for different samples with different concentrations of nitrogen vacancies. Reproduced with permission.[74] Copyright 2020, Wiley-VCH.

adsorbed N, weakening the N≡N bond (Fig. 9d). Simultaneously, plasmonic Au nanoparticles generate hot electrons under illumination, which are then transferred to the active vacancy sites for N_2 activation. The synergistic promotion of Au nanoparticles and nitrogen vacancies in the optimal Au/HCNS-NV composition leads to a high ammonia production rate.

As nitrogen vacancies play a crucial role in the photocatalytic ammonia synthesis, increasing the concentration of nitrogen vacancies is important to further improve the catalytic performance. Recently, Wu et al. conducted a study on Au-loaded g-C_3N_4 nanosheets (AuCNNVs), which demonstrated a high concentration of nitrogen vacancies. The results showed that Au NPs significantly promoted the generation of nitrogen vacancies, which was in line with the calculated nitrogen vacancy generation energy (Fig. 9e).[74] The electron paramagnetic resonance (EPR) spectroscopy results in Fig. 9f indicated that AuCNNVs had the highest concentration of nitrogen vacancies among the prepared catalysts. Moreover, Fig. 9g shows a positive correlation between the concentration of nitrogen vacancies and NH_3 yield. The LSPR effect of Au also improved the efficiency of visible light utilization in addition to the contribution of nitrogen vacancies. The integration of nitrogen vacancies and the LSPR effect of Au afforded a high ammonia yield of 93 μmol

g^{-1} without any sacrificial agent under visible-light illumination.

3.1.3. Metal site promoted N_2 activation. While vacancies in semiconductors can promote N_2 activation, the transfer of electrons between plasmonic metals and semiconductors is often inhibited by Schottky barriers. This leads to a reduced photocatalytic efficiency due to blocked electron transfer. Additionally, trapped electrons in vacancies can be easily quenched by H_2O or N_2 under photocatalytic conditions. In contrast to vacancies, metal alloys offer greater stability and can serve as effective active sites in plasmonic catalysis. For example, Martirez et al. evaluated transition metal (TM: Fe, Co, Ni, and Mo)-doped Au systems for plasmonic nitrogen fixation.[75] They found that the AuMo alloy showed the strongest binding to N_2, but it could easily be oxidized. In contrast, AuFe achieved desirable qualities for an NH_3 catalyst, including relative stability with respect to phase separation, reversibility of Fe oxidation and reduction, and reactivity toward N_2 adsorption and activation (Fig. 10a). The Fe component also contributed to states at the Fermi level of the alloys, enhancing N_2 dissociation over the active sites.

Compared to plasmonic noble metals like Au, Ag, or Ru, Cu has garnered significant interest due to its substantial LSPR
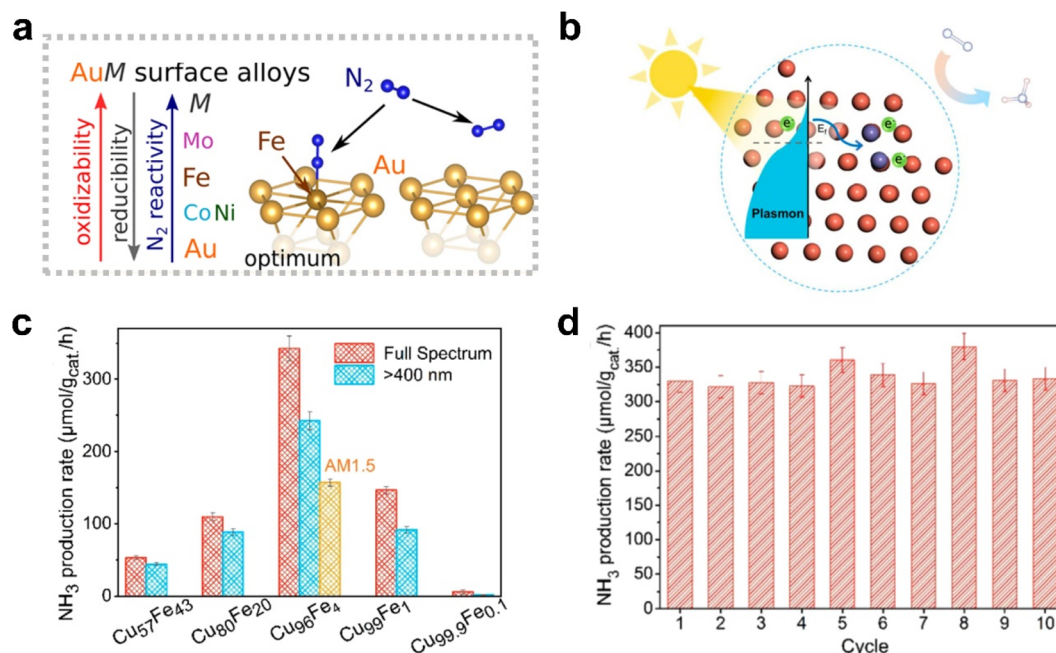
Fig. 10 (a) Schematic illustration of optimum AuM surface alloys. Reproduced with permission.[75] Copyright 2016, American Chemical Society. (b) The mechanism for plasmonic photocatalytic ammonia synthesis over the CuFe alloy. (c) NH_3 production rate over different CuFe alloys. (d) NH_3 production rate of $Cu_{96}Fe_4$ for 10 cycles. Reproduced with permission.[76] Copyright 2020, American Chemical Society.

effect in the visible light region and relative affordability. However, Cu nanoparticles are susceptible to corrosion in air and moisture, leading to challenges in the development of Cu-based catalysts with chemical stability. Recently, Hou *et al.* reported porous CuFe catalysts with varying Cu/Fe ratios by

selectively etching Fe elements from $Cu_{21}Fe_{79}$.[76] In this catalyst, the active Fe species for ammonia synthesis were promoted by plasmonic Cu, while surface Fe atoms acted as active sites for N_2 adsorption and activation (Fig. 10b). The optimal catalyst, $Cu_{96}Fe_4$, exhibited an ammonia production rate of 342 μmol g^{-1}
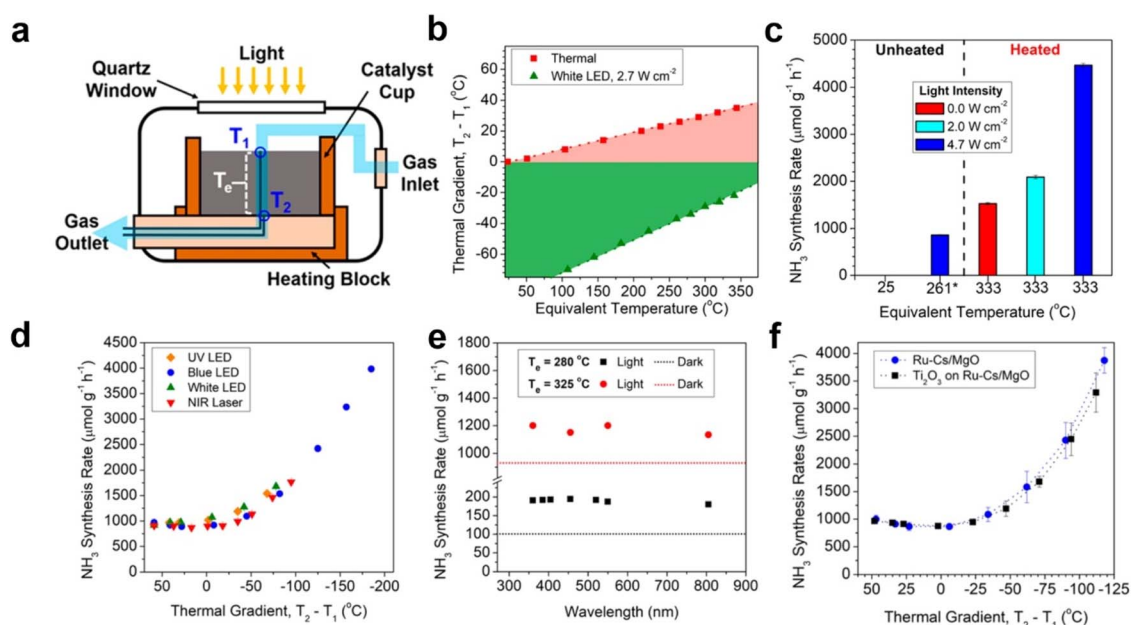

Fig. 11 (a) Schematic illustration of the reaction chamber for ammonia synthesis. (b) Thermal gradients under dark thermal and heated white light illumination. (c) NH_3 production rate under dark and illuminated conditions. (d) NH_3 production rate as a function of the thermal gradient. (e) Wavelength-dependent ammonia synthesis rates. (f) NH_3 production rate as a function of the thermal gradient for Ru–Cs/MgO and Ti_2O_3 on Ru–Cs/MgO. Reproduced with permission.[51] Copyright 2019, American Chemical Society.

Table 1 Summary of plasmonic-promoted catalysts for photocatalytic N_2 reduction. n.a.: not available

LSPR effects	Catalysts	T (°C)	Light source & bandwidth	Calibrated light intensity (W cm⁻²)	Catalyst mass (g)	Reaction phase	Reagents	Flow rate (mL min⁻¹)	$^{15}N_2$ confirmation	NH₃ yield (µmol g⁻¹ h⁻¹)	Method(s) of NH₃ quantification	AQE	STA	Ref.
Hot carrier injection	Au/TiO₂-OV	RT	Xe lamp (visible)	n.a.	0.1	Liquid	N₂ + H₂O	50	No	78.6	Indophenol-blue	0.82% (at 550 nm)	n.a.	53
	TiO₂/Au/a-TiO₂/	25	Xe lamp (420 nm filter)	0.1	n.a.	Liquid	N₂ + H₂O	20	No	0.01	Indophenol	n.a.	n.a.	54
	TiO₂/Au/K⁺	25	Xe lamp (UV-vis)	0.1	n.a.	Liquid	N₂ + H₂O	60	No	1020	Nessler's reagents and indophenol-blue	0.93% (at 550 nm)	n.a.	55
	CuFe	25	Xe lamp (full spectrum)	0.25	0.01	Liquid	N₂ + H₂O	Sealed (3 bar)	No	342	Nessler's reagents, indophenol-blue and ion chromatography	0.13% (at 550 nm)	0.06%	76
	Au/end-CeO₂	25	Diode laser (808 nm)	8	0.001	Liquid	N₂ + H₂O	5	No	114	Indophenol-blue	n.a.	n.a.	59
	Ti₃C₂Tₓ/TiO₂	25	Xe lamp (full spectrum)	0.25	0.01	Liquid	N₂ + H₂O	Sealed (1 bar)	No	422	Indophenol-blue and ion chromatography	0.07% (at 740 nm)	n.a.	68
	MoO₃₋ₓ	25	Xe lamp (full spectrum)	n.a.	0.05	Liquid	N₂ + H₂O	Sealed (1 bar)	No	328	Nessler's reagents, and ion chromatography	0.31% (at 808 nm)	n.a.	69
	SrMoO₄	20	Xe lamp (full spectrum)	n.a.	0.02	Liquid	N₂ + H₂O	100	No	3.9	Indophenol-blue	0.022% (at 500 nm)	n.a.	70
	Au/HCNS-NV	25	Xe lamp (full spectrum)	0.1	0.05	Liquid	N₂ + H₂O	50	No	783	Nessler's reagents	0.64% (at 550 nm)	0.03%	73
	AuCNNVs	25	Xe lamp (visible)	n.a.	0.05	Liquid	N₂ + H₂O	Sealed (1 bar)	No	184	Nessler's reagents	n.a	n.a.	74
Photo-thermal effect	Ru–Cs/MgO	333	Blue LED	4.7	0.02	Gas	N₂ + H₂	75	No	4464	Quadrupole mass spectrometer	n.a	n.a.	51
	α-Fe-110s	413	Xe lamp (full spectrum)	6.12	0.013	Gas	N₂ + H₂	60	Yes	1260	Ion chromatography	n.a	n.a.	78
	Ru/C	350	Xe lamp (full spectrum)	5	0.05	Gas	N₂ + H₂	30	No	1750	Nessler's reagents, and ion chromatography	n.a	n.a.	79
	K/Ru/TiO₂₋ₓHₓ	360	Xe lamp (full spectrum)	n.a.	0.1	Gas	N₂ + H₂	6	No	113	Nessler's reagent	n.a	n.a.	80
	Pt₁-Ptₙ-TiN	204	Blue LED (465)	0.6	0.1	Gas phase	N₂ + H₂	6	No	500	1H-NMR	0.03% (at 465 nm)	n.a.	81

Table 1 (Contd.)

LSPR effects	Catalysts	T (°C)	Light source & bandwidth	Calibrated light intensity (W cm^{-2})	Catalyst mass (g)	Reaction phase	Reagents	Flow rate (mL min^{-1})	$^{15}N_2$ confirmation	NH$_3$ yield (μmol g^{-1} h^{-1})	Method(s) of NH$_3$ quantification	AQE	STA	Ref.
Near field enhancement	AuRu$_{0.31}$	25	Xe lamp (full spectrum)	0.4	0.0002	Liquid	N$_2$ + H$_2$O	Sealed (2 bar)	Yes	101	Ion chromatography	0.017% (at 550 nm)	n.a.	82
	Ru-Vs-CoS/ CN	25	Xe lamp (full spectrum)	0	0.025	Liquid	N$_2$ + H$_2$O	Sealed (1 bar)	No	438	Indophenol-blue	1.28% (at 400 nm)	0.04%	83

h^{-1}, exceeding other reference catalysts under the same conditions (Fig. 10c). Furthermore, Cu$_{96}$Fe$_4$ retained ~100% of its initial activity after 10 cycles, implying excellent stability (Fig. 10d). The reaction's linear dependence on light intensity suggested that the process was driven by plasmonic hot electrons. This study represents a novel approach towards developing plasmonic photocatalysts for ammonia synthesis that are both stable and cost-effective using a Cu-based system.

3.2. Photothermal effect-assisted ammonia synthesis

Photoheating is a common occurrence in LSPR catalysis, driven by the mechanism of photothermal effect in plasmonic materials, where the decay of hot carriers leads to heat production through inelastic coulombic electron–electron scattering. This elevated local temperature improves the activation of reactant molecules, thereby facilitating chemical transformations. However, unlike the hot carrier and optical near-field-enhanced mechanisms, the photothermal effect cannot control product selectivity. Additionally, the photothermal effect and hot carriers are always generated simultaneously in one catalytic system, making it difficult to distinguish their thermochemical contributions in plasmonic photocatalysis.

Recently, Li *et al.* reported a novel photothermal plasmonic catalysis system that excludes nonthermal plasmonic effects such as the hot carrier-driven process.[51] In this system, light-induced thermal gradients primarily contributed to the activity enhancement of ammonia synthesis. The photocatalytic process is illustrated in Fig. 11a. A 3 mm-thick Ru–Cs/MgO catalyst was loaded into the reactor. The LED was positioned above the catalysts while a heating block beneath maintained the desired temperature. Under dark conditions, a positive thermal gradient ($\nabla T = T_2 - T_1$, where T_1 is the top-surface temperature and T_2 is the bottom-surface temperature) formed, whereas illumination caused the photoheating effect to generate a negative gradient (Fig. 11b). Under combined light and heat, the NH$_3$ production rate for the photo-thermal process (4464 μmol g^{-1} h^{-1}, at $T_e = 333$ °C and $\nabla T = -184$ °C) was consistently higher than under dark thermal conditions (1530 μmol g^{-1} h^{-1} at $T_e = 333$ °C and $\nabla T = +58$ °C) at the same temperature (Fig. 11c). Notably, the NH$_3$ production rate initially decreased slightly but then significantly increased with the shift from positive to negative thermal gradients (Fig. 11d). These findings underscore the critical role of negative thermal gradients in the ammonia synthesis reaction.

In general, molecules tend to move from the regions of high temperature to the regions of low temperature owing to thermophoretic forces. In the case of ammonia synthesis, a negative temperature gradient facilitates the adsorption and activation of reactants, such as N$_2$ and H$_2$, in a higher temperature region (T_1), while the product NH$_3$ moves to a lower temperature region (T_2) to prevent reverse decomposition. This negative gradient achieves a balance of high reaction activity and conversion yields. Interestingly, the illumination with different wavelengths has a similar effect on ammonia synthesis, unlike plasmonic photocatalysis driven by hot carriers (Fig. 11e). To confirm that the enhancement in ammonia synthesis is not due

to nonthermal effects such as hot carrier generation, a controlled experiment was conducted under indirect illumination using Ti_2O_3, a black photothermal material, on top of the catalysts to absorb all light and convert it to heat. The photothermal heating produced a negative gradient and provided similar enhancements in ammonia synthesis compared to direct illumination over Ru–Cs/MgO (Fig. 11f). Table 1 summarizes the plasmon-enhanced photocatalytic nitrogen reduction performance. It is obvious that Ru–Cs/MgO shows high activity towards photocatalytic ammonia synthesis, which is comparable to those catalysts employed in the thermal catalytic process. This observation confirms that photothermal heating dominates the ammonia synthesis enhancement rather than hot carrier generation. This study offers a universal and scalable strategy for catalysing various exothermic chemical reactions.

3.3. The optical near-field assisted ammonia synthesis

Near-field enhancement is an effective approach to promote plasmonic photocatalysis. Plasmonic materials absorb light under illumination, leading to the separation of hot electrons and holes, which result in a localized increase in the density of photonic states, known as near field. The interaction derived from near field facilitates the activation of reactants on the surface of catalysts. For ammonia synthesis, the primary challenge lies in N_2 activation due to the extremely large bonding energy of the N≡N triple bond (941 kJ mol^{-1}).[77] The plasmonic materials enable the cleavage of the N≡N bond through indirect and direct hot carrier transfer into the adsorbate.[30] The former method involves hot carriers transferring to the lowest unoccupied molecular orbital of the adsorbate on the surface of catalysts, while the latter involves direct hot carrier transferring from plasmonic materials to the hybridized metal–adsorbate interface. Different from the indirect mechanism that takes place after the generation of hot carriers, the direct mechanism occurs at the process of plasmon excitation. However, the direct pathway is uncommon in many reactions because the surface orbital hybridization requires an intense metal/adsorbate interaction.

An intriguing study by Xiong *et al.* demonstrated photocatalytic nitrogen fixation in pure water under mild conditions, highlighting the important role of direct energy transfer in
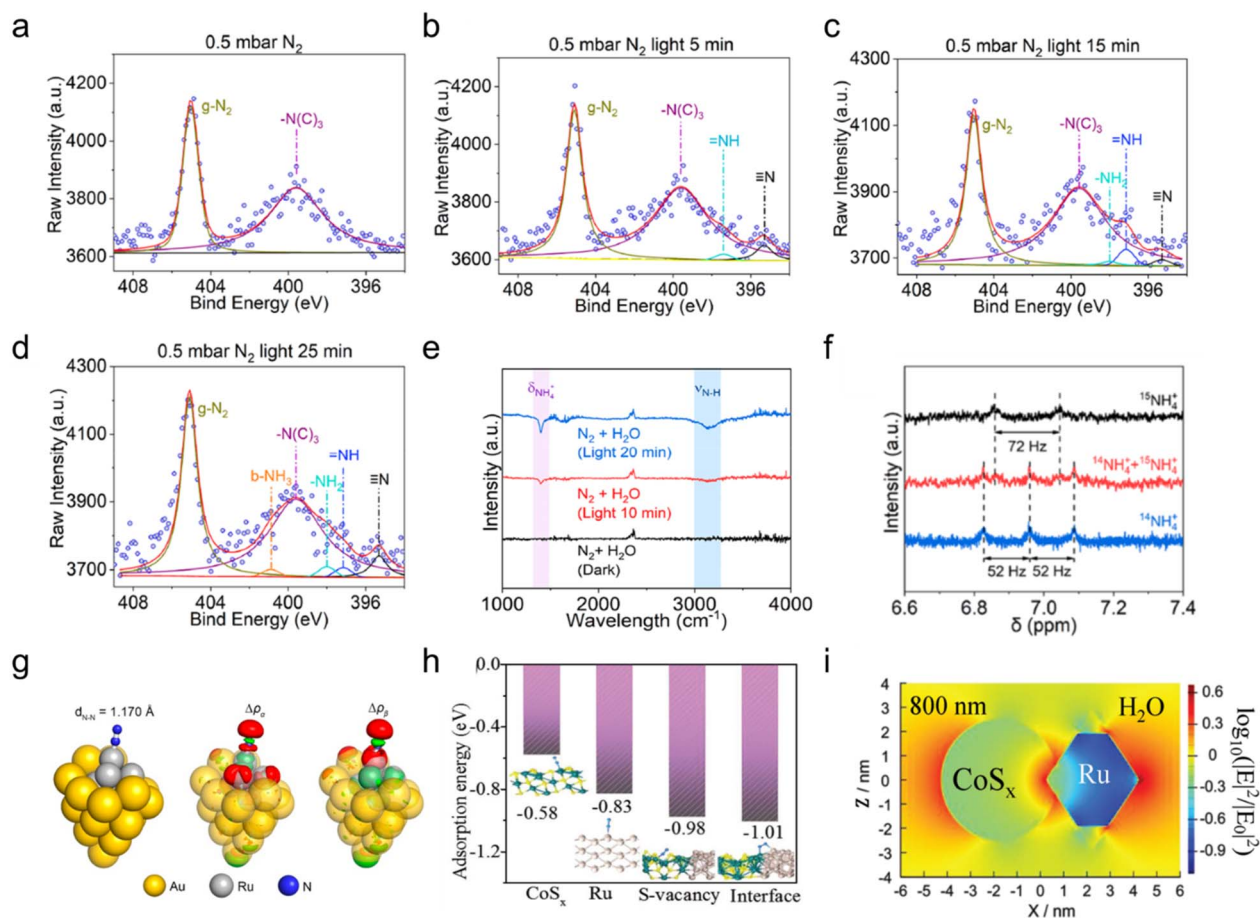

Fig. 12 (a)–(d) N 1s XPS spectra of AuRu$_{0.31}$. (e) *In situ* DRIFTS spectra recorded for $N_2 + H_2O$ over AuRu$_{0.31}$ under irradiation conditions. (f) ^{1}H NMR spectra of solution after the N_2 fixation reaction in the $^{15}N_2$, $^{15}N_2 + ^{14}N_2$, or $^{14}N_2$ atmosphere. (g) Optimized structures of N_2 adsorbed on the AuRu cluster. Reproduced with permission.[82] Copyright 2019, American Chemical Society. (h) Adsorption energies of N_2 on different sites. FDTD electric field distribution. (i) FDTD electric field distribution at Ru/CoS$_x$ nanoparticle (800 nm irradiation) observed from γ-axis (vertical to incident light). Reproduced with permission.[83] Copyright 2019, Wiley-VCH.

AuRu core-antenna nanostructures.[82] *In situ* Near-Ambient Pressure X-ray Photoelectron Spectroscopy (NAP-XPS) analysis revealed a N 1s peak attributed to atomic nitrogen (Fig. 12a–d), while no spectroscopic signatures for associative intermediates (*e.g.*, $*N_2H_x$) were detected by Diffuse Reflectance Infrared Fourier Transform Spectroscopy (DRIFTS) (Fig. 12e). Additionally, [1]H Nuclear Magnetic Resonance (^{1}H NMR) spectra using $^{15}N_2$ confirmed that the produced NH_3 originated from N_2 gas (Fig. 12f). Based on these results, the authors proposed that the reaction proceeds *via* a dissociative mechanism. First-principles calculations indicated that photo-induced plasmonic near-fields play a crucial role in N_2 activation. According to the calculations, hot electron transfer caused only minimal N≡N bond elongation, while applying a local electric field resulted in significant bond stretching (Fig. 12g). Combining the effects of hot electrons and local electric fields, a proposed reaction mechanism suggests that the N_2 molecule is chemisorbed at Ru sites to form a highly hybridized Ru–N_2 complex, facilitated by the local electric field generated from plasmonic Au excitation. This study emphasizes the potential contribution of the plasmonic near-field to N_2 activation. However, definitive evidence for a dissociative mechanism in this system requires further substantiation, as the inability to detect associative intermediates could be due to their low surface coverage or transient nature.

Future investigations utilizing time-resolved spectroscopy and isotope scrambling experiments with $^{14}N_2/^{15}N_2$ mixtures could provide more conclusive mechanistic evidence. Nonetheless, this work underscores the significance of local electric fields and presents a novel platform for designing advanced plasmonic catalysts for ammonia synthesis.

In many cases, N_2 adsorption occurs through a terminal end-on mode in ammonia synthesis, in which the N atom solely binds with active metal atoms to accept electrons. However, recent studies have shown that a bridging adsorption mode is more favourable for N_2 activation in homogeneous catalysis.[83] For example, a heterojunction of Ru/CoS_x in g-C_3N_4 nanosheets was reported to achieve N_2 activation through a bridging adsorption mode. In this system, the N atoms were adsorbed to the Ru–Co centre with a lower adsorption energy than end-on adsorption to a Ru or Co site, or a S vacancy (Fig. 12h). Such side-on bridging adsorption contributed to the polarization of N≡N bonds. Simultaneously, the Schottky barrier between Ru and CoS_x endows the interface with electron transfer from CoS_x to Ru, and the S vacancies of CoS_x can broaden the light absorption range and serve as additional electron donors for light-excited electrons to promote N_2 activation. In addition, the local electric field enhanced by the

LSPR derived from plasmonic Ru nanoparticles accelerates charge separation and transfer, leading to more efficient N_2 activation (Fig. 12i). This work emphasizes the importance of controlling the N_2-coordination environment for the improvement of ammonia synthesis performance.

4. Outlook

Plasmonic photocatalysis offers an intriguing alternative for ammonia synthesis under mild conditions, contrasting sharply with the energy-intensive Haber–Bosch process. As summarized in Table 2, when compared to other emerging technologies, such as thermal catalysis with renewable H_2, plasma catalysis, and electrochemical nitrogen reduction, the distinct advantage of plasmonic photocatalysis lies in its ability to directly harness solar energy. However, its current development is hindered by extremely low catalytic performance, characterized by low Space-Time Yield (STY) and energy efficiency. These limitations arise from fundamental challenges, including low quantum yields and rapid charge carrier recombination. This comparative analysis highlights that no alternative route currently rivals the scaled efficiency of Haber–Bosch. Since plasmonic photocatalytic ammonia synthesis is still in its early stages, significant effort is needed to advance this technology. Accordingly, we outline the forthcoming challenges in plasmonic photocatalytic ammonia synthesis and propose potential directions for future research.

4.1. Design of plasmonic catalysts for ammonia synthesis

4.1.1. Size and shape effects for plasmonic materials. The LSPR phenomenon in plasmonic nanoparticles is highly dependent on both particle size and shape. These parameters influence the generation of hot carriers, the intensity and distribution of local electric fields, and the extent of photo-heating. Generally, smaller nanoparticles with more energetic hot carriers are thought to exhibit higher catalytic activity. However, smaller nanoparticles also have lower absorption cross-sections, resulting in a reduced photothermal effect. For catalytic reactions where local thermal activation is critical to the rate-determining step, focusing solely on minimizing nanoparticle size may inadvertently diminish the necessary photothermal contribution, ultimately lowering the overall reaction rate. Thus, achieving a precise balance to quantitatively predict the optimal nanoparticle size is essential for future progress.

Morphology is also a key factor in determining the LSPR effects of plasmonic catalysts. Previous studies have shown that

Table 2 Comparison of several catalytic systems for energy efficiency, STY, scalability, and technology readiness

Catalytic systems	Plasmonic photocatalysis	Thermal catalysis	Plasma catalysis	Electrochemical NRR
Energy efficiency	Very low	Moderate to high	Low	Very low
Space-time yield	Low	High	Low to moderate	Low
Scalability	Limited	Excellent	Limited	Limited
Technology readiness	Low	High	Low	Low

nanoparticle shape can significantly influence the region of light absorption. However, current research has mainly concentrated on non-anisotropic structures. Nanoparticles with sharp, flat, or elongated geometries, such as bipyramids or branched nanostructures, are known to generate hot electrons and holes more efficiently. Designing plasmonic structures with specific shapes is therefore an important direction for future research. Moreover, the areas of strongest field enhancement often correspond to crystallographically unstable regions that are susceptible to structural reconstruction or deactivation under reaction conditions. As a result, morphological design must consider not only the spatial distribution and dynamic evolution of electromagnetic hotspots and catalytic active sites but also the structural stability of the nanoparticles.

Given these considerations, future research should focus on creating standardized libraries of plasmonic nanocrystals, including nanorods, bipyramids, core–shell structures, and gap antennas, with precisely controlled geometric parameters such as dimensions, aspect ratios, and tip curvatures. Through systematic optical characterization and catalytic testing of these libraries, we can more accurately determine how specific geometric features influence hot carrier energy distribution, local electric field profiles (both intensity and spatial localization), and photothermal conversion efficiency.

4.1.2. Rational design of plasmonic hybrid structures.

Although plasmonic nanoparticles efficiently generate hot carriers under irradiation, their use is limited by short carrier lifetimes and rapid electron–hole recombination. Constructing hybrid structures is a cornerstone strategy for overcoming these intrinsic limitations. By creating interfaces between distinct components, spatial separation of electrons and holes is achieved, reducing recombination and directing carriers toward specific redox processes. While the fundamental principles of Schottky and ohmic contacts governing carrier transfer are well established, recent research highlights that rational nanostructural design unlocks significant performance breakthroughs.

As discussed in Section 3, several recent examples illustrate advanced strategies in hybrid design. For instance, site-selective growth of CeO_2 at the ends of Au nanorods creates a spatial configuration that separates the reduction site (CeO_2 with oxygen vacancies) from the oxidation site (Au), markedly enhancing charge separation. Similarly, Au nanoparticles encapsulated in hollow carbon nitride within core–shell structures allow the plasmonic core to function as an embedded antenna, while the shell offers active sites and protection. Bimetallic plasmonic cores (e.g., AuRu) with tailored electronic structures further demonstrate how optimizing the plasmonic component itself improves hot carrier generation and transfer. These examples show a shift from simple hybridization to precise nanoscale engineering of geometry and the electronic structure. Looking forward, several key points should be considered for the design of plasmonic materials.

(1) Precision in interface and alloy engineering: Future effort must go beyond bulk heterojunctions. Atomic-level control over the interface structure, achieved through techniques like atomic layer deposition, and the design of alloys or intermetallic compounds will allow for fine-tuning the Schottky barrier height and the dynamics of hot carrier injection.

(2) Expanding the material varieties beyond oxides: While metal-oxide semiconductors have dominated, the exploration of hybrids with non-oxide materials, such as nitrides, phosphides, sulfides, and carbides, presents a vast and untapped opportunity. These materials often possess superior electrical conductivity, narrower bandgaps, and different types of vacancies (e.g., N, S, P, and C vacancies) that could lead to novel adsorption and activation pathways for N_2.

(3) Integration with theory and data science: the multi-combination of materials, morphologies, and interfaces is immense. The integration of multi-scale theoretical simulations with machine-learning-guided catalyst design will be indispensable for identifying the most promising hybrid configurations and accelerating the discovery process.

4.1.3. Catalyst stability in design.

Beyond efficiency, catalyst stability is a major bottleneck for real-world applications. Current studies usually report only short-term catalytic performance, which does not reflect material behavior over extended use. Future design must prioritize stability from the outset and apply unified standards for durability assessment.

Catalyst deactivation is a complex process affected by photochemical corrosion, thermal sintering or reconstruction, and surface poisoning. Strategies to enhance robustness include:

(1) Encapsulating the plasmonic metal core with an inert yet conductive or mesoporous shell (e.g., silica, titania, carbon, etc.) is a promising strategy. An ideal shell should: (i) physically isolate the core from the harsh reaction environment, preventing corrosion and sintering; (ii) allow free diffusion of reactants and products; and (iii) effectively passivate high-surface-energy facets without severely compromising the charge transfer efficiency.

(2) Constructing alloys or intermetallic compounds between the active plasmonic metal (e.g., Cu) and a more stable metal (e.g., Au, Pd, Pt, etc.) can intrinsically enhance the stability from both electronic and thermodynamic perspectives. The alloying component not only modulates the electronic states to optimize reaction pathways but also raises the activation barrier for corrosion reactions. For example, constructing AuCu alloys can effectively suppress Cu leaching while potentially maintaining or even enhancing catalytic performance through synergistic effects.

(3) Selecting reducible supports (e.g., TiO_{2-x}, MoO_{3-x}, etc.) that can form strong interactions with plasmonic nanoparticles, or those that induce an SMSI effect under reaction conditions, can pin the nanoparticles and prevent their migration and sintering. In some cases, an ultra-thin overlayer formed on the nanoparticle surface via SMSI can provide protection without completely blocking the reaction.

4.2. Operando characterization and theoretical methods

The complex interplay in plasmonic catalysis, involving the hot carrier, local near field, and photothermal effect, cannot be easily determined by conventional characterization methods. Operando probing of the catalyst under catalytic conditions is essential. In many cases, applying only single technique is not

enough. Therefore, developing multiple *operando* techniques to investigate the mechanism is of great importance. We propose a coordinated approach where specific mechanistic questions are addressed by the most suitable combination of techniques.

To decipher morphological and structural dynamics, such as light-induced sintering, or facet evolution of plasmonic nanoparticles under reactive environments, techniques like Environmental Transmission Electron Microscopy (ETEM) or Optically coupled TEM (OTEM) are indispensable.[84] They provide direct, real-time visual evidence at near-atomic resolution, revealing how the catalyst's physical structure adapts and potentially degrades during operation. For uncovering surface chemistry and reaction intermediates, methods such as Near-Ambient Pressure X-ray Photoelectron Spectroscopy (NAP-XPS) and *operando* Fourier-Transform Infrared (FTIR) spectroscopy are paramount. NAP-XPS can directly identify the chemical states of catalyst surfaces and adsorbed species, while *operando* FTIR tracks the evolution of key reaction intermediates, together with clarifying the reaction pathway and active sites.

Critically, understanding the plasmonic enhancement itself requires probing the local electromagnetic field and obtaining molecular fingerprints at the nanoscale. This is the exclusive domain of Surface- and Tip-Enhanced Raman Spectroscopy (SERS/TERS). These techniques provide dramatically enhanced vibrational signals, allowing them to probe molecular adsorption and reaction pathways precisely at the electromagnetic "hot spots" directly correlating enhanced fields with catalytic activity. Finally, hot carriers occur on femtosecond to picosecond timescales, and they cannot be observed by conventional methods. Ultrafast transient absorption spectroscopy is an effective tool capable of directly tracking these processes, quantifying the efficiency of initial charge carrier separation and injection, which is the very foundation of plasmon-mediated photocatalysis.

Theoretical research must keep pace with these experimental advances. Traditional Density Functional Theory (DFT), while invaluable for modeling ground-state chemistry and adsorption energies, is inherently inadequate for describing the non-equilibrium, excited-state processes that define plasmonic catalysis. Its limitations in dealing with excited states and strong electronic correlations can lead to spurious conclusions. Therefore, the development and application of higher-level, multi-reference quantum chemical methods, such as emerging theories such as multiconfigurational n-electron valence second-order perturbation theory (e-NEVPT2) and embedded complete-active-space second-order perturbation theory (emb-CASPT2), are critical.[85,86] These methods can more accurately describe the excited potential energy surfaces and charge transfer states involved in plasmon-driven reactions, providing a reliable theoretical framework to interpret complex *operando* data and guide catalyst design.

4.3. Metrics and standardization for plasmonic photocatalysis

Plasmonic photocatalytic ammonia synthesis is still in its infancy, and there is currently no standardized method for assessing the performance of different plasmonic photocatalysts. Therefore, establishing rigorous benchmarks is essential to standardize ammonia synthesis rate measurements.

Compared to thermal catalysis for ammonia synthesis, plasmonic photocatalytic processes display significantly lower activity levels, making accurate detection of NH_3 yield challenging due to various pollution sources. To tackle this issue, we provide a "Decision tree for artifact exclusion" box containing practical steps (Fig. 13).

Before testing, rigorous controlled experiments are essential. Catalytic performance should be evaluated in the dark, without a catalyst, in an Ar atmosphere without N_2 and H_2 to rule out false positives, including ambient NH_3/NO_x, nitrogen leaching from supports and sacrificial reagents. When NH_3 production exceeds the background level, conducting a ^{15}N isotope experiments is strongly recommended to eliminate pollution sources. Additionally, the current method for detecting the NH_3 yield primarily relies on spectrometric techniques, specifically Nessler's reagent. Future efforts should include multi-method approaches for NH_3 quantification, facilitating comparisons with reported catalysts. For nitrogen-containing catalysts, performing post-reaction XPS or Electron Energy Loss Spectroscopy (EELS) is crucial to rule out lattice nitrogen consumption. Only after passing these verification steps can the reported activity be deemed credible.

For photocatalytic systems, inconsistencies in reaction parameters, such as illumination source, wavelength range and intensity, solution pH, catalyst loading, and sacrificial oxidants, present significant obstacles to comparative studies. Thus, there is an urgent need to develop standard reactors for photocatalysis. These reactors must be designed to ensure a uniform and well-defined light source, incorporate effective heat-sinking to separate genuine thermal effects from bulk photothermal heating, and enable precise control over mass transport. Simultaneously, a strict set of parameters should be mandated for all publications. Standardizing experimental procedures and performance metrics is essential for enhancing data reliability, thereby paving the way for the development of
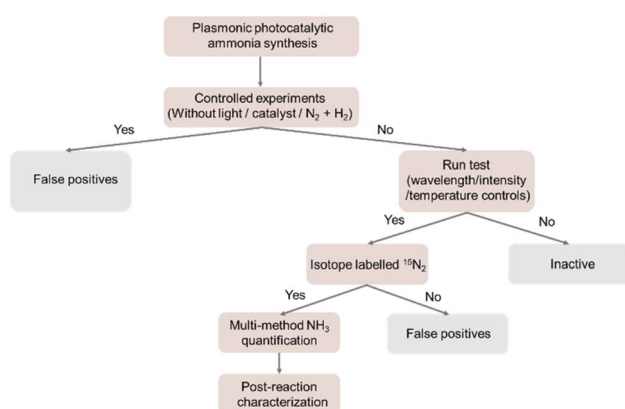

Fig. 13 Decision tree for artefact exclusion in plasmonic photocatalysis.

nitrogen fixation demonstrators, pilot plants, and ultimately solar ammonia refineries.

Author contributions

W.-Q. Li: investigation, conceptualization, writing-original draft, visualization, and writing-review & editing; M. Xu, G. Chen, X. Chen: writing-review & editing; J.-S. Chen: funding acquisition and supervision; T.-N. Ye: conceptualization, writing-review & editing, funding acquisition and supervision.

Conflicts of interest

The authors declare no competing interests.

Data availability

No primary research results, software or code have been included and no new data were generated or analysed as part of this review.

Acknowledgements

References

1 F. Robert, *Science*, 2018, **361**, 120–123.
2 L. Hui, Y. Xue, H. Yu, Y. Liu, Y. Fang, C. Xing, B. Huang and Y. Li, *J. Am. Chem. Soc.*, 2019, **141**, 10677–10683.
3 D. R. MacFarlane, P. V. Cherepanov, J. Choi, B. H. R. Suryanto, R. Y. Hodgetts, J. M. Bakker, F. M. Ferrero Vallana and A. N. Simonov, *Joule*, 2020, **4**, 1186–1205.
4 Q. Wang, J. Guo and P. Chen, *J. Energy Chem.*, 2019, **36**, 25–36.
5 N. Gruber and J. N. Galloway, *Nature*, 2008, **451**, 293–296.
6 S. L. Foster, S. I. P. Bakovic, R. D. Duda, S. Maheshwari, R. D. Milton, S. D. Minteer, M. J. Janik, J. N. Renner and L. F. Greenlee, *Nat. Catal.*, 2018, **1**, 490–500.
7 L. Huang, L. Cheng, T. Ma, J. J. Zhang, H. Wu, J. Su, Y. Song, H. Zhu, Q. Liu, M. Zhu, Z. Zeng, Q. He, M. K. Tse, D. t. Yang, B. I. Yakobson, B. Z. Tang, Y. Ren and R. Ye, *Adv. Mater.*, 2023, **35**, 2211856.
8 B. Chang, Z. Cao, Y. Ren, C. Chen, L. Cavallo, F. Raziq, S. Zuo, W. Zhou, Y. Han and H. Zhang, *ACS Nano*, 2023, **18**, 288–298.
9 H. Li, J. Shang, Z. Ai and L. Zhang, *J. Am. Chem. Soc.*, 2015, **137**, 6393–6399.
10 H. Wang, Y. Li, C. Li, K. Deng, Z. Wang, Y. Xu, X. Li, H. Xue and L. Wang, *J. Mater. Chem. A*, 2019, **7**, 801–805.
11 L. Collado, A. H. Pizarro, M. Barawi, M. G. Tecedor, M. Liras and V. A. P. O' Shea, *Chem. Soc. Rev.*, 2024, **53**, 11334.
12 Z. Zhao, R. Tan, Y. Kong, Z. Zhang, S. Qiu, X. Mu and L. Li, *Angew. Chem., Int. Ed.*, 2023, **62**, e202303629.
13 A. Banerjee, B. D. Yuhas, E. A. Margulies, Y. Zhang, Y. Shim, M. R. Wasielewski and M. G. Kanatzidis, *J. Am. Chem. Soc.*, 2015, **137**, 2030–2034.
14 W. Wang, H. Zhang, S. Zhang, Y. Liu, G. Wang, C. Sun and H. Zhao, *Angew. Chem., Int. Ed.*, 2019, **58**, 16644–16650.
15 Y. Shi, Z. Zhao, D. Yang, J. Tan, X. Xin, Y. Liu and Z. Jiang, *Chem. Soc. Rev.*, 2023, **52**, 6938–6956.
16 J. Zheng, L. Lu, K. Lebedev, S. Wu, P. Zhao, I. J. McPherson, T.-S. Wu, R. Kato, Y. Li, P.-L. Ho, G. Li, L. Bai, J. Sun, D. Prabhakaran, R. A. Taylor, Y.-L. Soo, K. Suenaga and S. C. E. Tsang, *Chem Catal.*, 2021, **1**, 162–182.
17 G. Zhang, T. Dai, Y. Wang, Y. Meng, B. Xie, Z. Ni and S. Xia, *Appl. Catal., B*, 2021, **288**, 119990.
18 N. N. Vu, S. Kaliaguine and T. O. Do, *ChemSusChem*, 2020, **13**, 3967–3991.
19 X. Zhang, X. Li, D. Zhang, N. Q. Su, W. Yang, H. O. Everitt and J. Liu, *Nat. Commun.*, 2017, **8**, 14542.
20 P. Zhang, T. Wang and J. Gong, *Adv. Mater.*, 2015, **27**, 5328–5342.
21 H. Ren, J.-L. Yang, W.-M. Yang, H.-L. Zhong, J.-S. Lin, P. M. Radjenovic, L. Sun, H. Zhang, J. Xu, Z.-Q. Tian and J.-F. Li, *ACS Mater. Lett.*, 2020, **3**, 69–76.
22 F. Tong, X. Liang, F. Ma, X. Bao, Z. Wang, Y. Liu, P. Wang, H. Cheng, Y. Dai, B. Huang and Z. Zheng, *ACS Catal.*, 2021, **11**, 3801–3809.
23 D. Mittal, M. Ahlawat and V. Govind Rao, *Adv. Mater. Interfaces*, 2022, **9**, 2102383.
24 S. Swaminathan, V. G. Rao, J. K. Bera and M. Chandra, *Angew. Chem., Int. Ed.*, 2021, **60**, 12532–12538.
25 A. Bansal, J. S. Sekhon and S. S. Verma, *Plasmonics*, 2013, **9**, 143–150.
26 A. Gelle, T. Jin, L. de la Garza, G. D. Price, L. V. Besteiro and A. Moores, *Chem. Rev.*, 2020, **120**, 986–1041.
27 B. Puértolas, M. Comesaña-Hermo, L. V. Besteiro, M. Vázquez-González and M. A. Correa-Duarte, *Adv. Energy Mater.*, 2022, **12**, e2103909.
28 E. A. Monyoncho and M. Dasog, *Adv. Energy Sustainability Res.*, 2021, **2**, e2000055.
29 A. Choudhary, A. Halder, P. Aggarwal and V. Govind Rao, *Commun. Mater.*, 2024, **5**, 69.
30 D. Mateo, J. L. Cerrillo, S. Durini and J. Gascon, *Chem. Soc. Rev.*, 2021, **50**, 2173–2210.
31 M. Ahlawat, D. Mittal and V. Govind Rao, *Commun. Mater.*, 2021, **2**, 114.
32 S. Chavez, V. G. Rao and S. Linic, *Faraday Discuss.*, 2019, **214**, 441–453.
33 U. Aslam, V. G. Rao, S. Chavez and S. Linic, *Nat. Catal.*, 2018, **1**, 656–665.
34 V. G. Rao, U. Aslam and S. Linic, *J. Am. Chem. Soc.*, 2018, **141**, 643–647.
35 T. Shen, J.-C. Ren, X. Liu, S. Li and W. Liu, *J. Am. Chem. Soc.*, 2019, **141**, 3110–3115.

36 C. Bauer, J. P. Abid, D. Fermin and H. H. Girault, *J. Chem. Phys.*, 2004, **120**, 9302–9315.

37 M. R. Lukatskaya, O. Mashtalir, C. E. Ren, Y. D. Agnese, P. Rozier, P. L. Taberna, M. Naguib, P. Simon, M. W. Barsoum and Y. Gogotsi, *Science*, 2013, **341**, 1502–1505.

38 S. Yu, A. J. Wilson, G. Kumari, X. Zhang and P. K. Jain, *ACS Energy Lett.*, 2017, **2**, 2058–2070.

39 L. Ding, X. Zhu, Y. Wang, B. Shi, X. Ling, H. Chen, W. Nan, A. Barrett, Z. Guo, W. Tao, J. Wu and X. Shi, *Nano Lett.*, 2017, **17**, 6790–6801.

40 A. Politano, P. Argurio, G. Di Profio, V. Sanna, A. Cupolillo, S. Chakraborty, H. A. Arafat and E. Curcio, *Adv. Mater.*, 2017, **29**, e1603504.

41 S. Lu, F. Liu, P. Qiu, M. Qiao, Y. Li, Z. Cheng, N. Xue, X. Hou, C. Xu, Y. Xiang, F. Peng and Z. Guo, *Chem. Eng. J.*, 2020, **379**, e122382.

42 Y. Shao, Z. Jiang, Y. Zhang, T. Wang, P. Zhao, Z. Zhang, J. Yuan and H. Wang, *ACS Nano*, 2018, **12**, 11704–11710.

43 A. O. Govorov and H. H. Richardson, *Nanotoday*, 2007, **2**, 30–38.

44 C. Le, W. Luo, B. Fang, J. Sun, Y. Chen, X. Feng and W. Zhang, *Mater. Today Commun.*, 2022, **30**, e103173.

45 A. O. Govorov, W. Zhang, T. Skeini, H. H. Richardson, J. Lee and N. A. Kotov, *Nanoscale Res. Lett.*, 2006, **1**, 84–90.

46 E.-R. Newmeyer, Y. Wang, Z. A. Long, J. D. North, Y. Shi and D. F. Swearer, *J. Am. Chem. Soc.*, 2025, **147**, 11789–11799.

47 Y. Yang, H. Jia, N. Hu, M. Zhao, J. Li, W. Ni and C.-y. Zhang, *J. Am. Chem. Soc.*, 2024, **146**, 7734–7742.

48 X. Yin, D. Gao, J. Zhang, H. García, J. Yu and H. Yu, *J. Am. Chem. Soc.*, 2025, **147**, 34881–34890.

49 R. C. Elias, B. Yan and S. Linic, *J. Am. Chem. Soc.*, 2024, **146**, 29656–29663.

50 J. Jia, H. Wang, Z. Lu, P. G. O'Brien, M. Ghoussoub, P. Duchesne, Z. Zheng, P. Li, Q. Qiao, L. Wang, A. Gu, F. M. Ali, Y. Dong, Q. Wang, K. K. Ghuman, T. Wood, C. Qian, Y. Shao, C. Qiu, M. Ye, Y. Zhu, Z. H. Lu, P. Zhang, A. S. Helmy, C. V. Singh, N. P. Kherani, D. D. Perovic and G. A. Ozin, *Adv. Sci.*, 2017, **4**, 1700252.

51 X. Li, X. Zhang, H. O. Everitt and J. Liu, *Nano Lett.*, 2019, **19**, 1706–1711.

52 H. Song, X. Meng, T. D. Dao, W. Zhou, H. Liu, L. Shi, H. Zhang, T. Nagao, T. Kako and J. Ye, *ACS Appl. Mater. Interfaces*, 2017, **10**, 408–416.

53 J. Yang, Y. Guo, R. Jiang, F. Qin, H. Zhang, W. Lu, J. Wang and J. C. Yu, *J. Am. Chem. Soc.*, 2018, **140**, 8497–8508.

54 C. Li, T. Wang, Z. J. Zhao, W. Yang, J. F. Li, A. Li, Z. Yang, G. A. Ozin and J. Gong, *Angew. Chem., Int. Ed.*, 2018, **57**, 5278–5282.

55 T.-A. Bu, Y.-C. Hao, W.-Y. Gao, X. Su, L.-W. Chen, N. Zhang and A.-X. Yin, *Nanoscale*, 2019, **11**, 10072–10079.

56 P. Li, Z. Zhou, Q. Wang, M. Guo, S. Chen, J. Low, R. Long, W. Liu, P. Ding, Y. Wu and Y. Xiong, *J. Am. Chem. Soc.*, 2020, **142**, 12430–12439.

57 H. Yin, Z. Chen, Y. Peng, S. Xiong, Y. Li, H. Yamashita and J. Li, *Angew. Chem., Int. Ed.*, 2022, **61**, e202114242.

58 L. D. Chen, M. Urushihara, K. Chan and J. K. Nørskov, *ACS Catal.*, 2016, **6**, 7133–7139.

59 H. Jia, A. Du, H. Zhang, J. Yang, R. Jiang, J. Wang and C. Y. Zhang, *J. Am. Chem. Soc.*, 2019, **141**, 5083–5086.

60 C. Feng, F. Raziq, M. Hu, H. Huang, Z. P. Wu, S. Zuo, J. Luo, Y. Ren, B. Chang, D. Cha, S. Ayirala, A. Al-Yousef, T. D. Dao and H. Zhang, *Adv. Energy Mater.*, 2024, **14**, 2303792.

61 Q. Tang, Z. Zhou and P. Shen, *J. Am. Chem. Soc.*, 2012, **134**, 16909–16916.

62 M. Mahato, J. Kim, M.-J. Lee, S. Jo, G. Kim, S. Nam, J.-S. Kim, V. H. Nguyen, . Garai, H. Yoo, D. Saatchi, Z. Ullah, C. W. Ahn, Y. Gogotsi and I.-K. Oh, *Adv. Mater.*, 2025, **37**, 2500479.

63 Z. Wang, H. Kim and H. N. Alshareef, *Adv. Mater.*, 2018, **30**, 1706656.

64 Y. Xia, T. S. Mathis, M. Q. Zhao, B. Anasori, A. Dang, Z. Zhou, H. Cho, Y. Gogotsi and S. Yang, *Nature*, 2018, **557**, 409–412.

65 D. B. Velusamy, J. K. El-Demellawi, A. M. El-Zohry, A. Giugni, S. Lopatin, M. N. Hedhili, A. E. Mansour, E. D. Fabrizio, O. F. Mohammed and H. N. Alshareef, *Adv. Mater.*, 2019, **31**, e1807658.

66 K. Chaudhuri, M. Alhabeb, Z. Wang, V. M. Shalaev, Y. Gogotsi and A. Boltasseva, *ACS Photonics*, 2018, **5**, 1115–1122.

67 D. A. Panova, G. I. Tselikov, G. A. Ermolaev, A. V. Syuy, D. S. Zimbovskii, O. O. Kapitanova, D. I. Yakubovsky, A. B. Mazitov, I. A. Kruglov, A. A. Vyshnevyy, A. V. Arsenin and V. S. Volkov, *Opt. Lett.*, 2024, **49**, 1.

68 T. Hou, Q. Li, Y. Zhang, W. Zhu, K. Yu, S. Wang, Q. Xu, S. Liang and L. Wang, *Appl. Catal., B*, 2020, **273**, 119072.

69 H. Wu, X. Li, Y. Cheng, Y. Xiao, R. Li, Q. Wu, H. Lin, J. Xu, G. Wang, C. Lin, X. Chen and Y. Wang, *J. Mater. Chem. A*, 2020, **8**, 2827–2835.

70 Q. Li, Z. Zhao, X. Bai, X. Tong, S. Yue, J. Luo, X. Yu, Z. Wang, Z. Wang, P. Li, Y. Liang and Z. Wang, *Chin. J. Catal.*, 2021, **42**, 1763–1771.

71 T. N. Ye, S. W. Park, Y. Lu, J. Li, M. Sasase, M. Kitano, T. Tada and H. Hosono, *Nature*, 2020, **583**, 391–395.

72 Z. Wang, X. Hu, Z. Liu, G. Zou, G. Wang and K. Zhang, *ACS Catal.*, 2019, **9**, 10260–10278.

73 Y. Guo, J. Yang, D. Wu, H. Bai, Z. Yang, J. Wang and B. Yang, *J. Mater. Chem. A*, 2020, **8**, 16218–16231.

74 S. Wu, Z. Chen, K. Liu, W. Yue, L. Wang and J. Zhang, *ChemSusChem*, 2020, **13**, 3455–3461.

75 J. M. Martirez and E. A. Carter, *ACS Nano*, 2016, **10**, 2940–2949.

76 T. Hou, L. Chen, Y. Xin, W. Zhu, C. Zhang, W. Zhang, S. Liang and L. Wang, *ACS Energy Lett.*, 2020, **5**, 2444–2451.

77 S. Gambarotta and J. Scott, *Angew. Chem., Int. Ed.*, 2004, **43**, 5298–5308.

78 Y. Yang, P. Wang, X. Zhang, S. Wang, X. Ding, H. Ma, H. Wang, Y. Li, B. Jiang, H. Song, X. Hai, Y. Lu, H. Chen and J. Ye, *Angew. Chem., Int. Ed.*, 2024, **136**, e202408309.

79 X. Bian, Y. Zhao, G. I. N. Waterhouse, Y. Miao, C. Zhou, L. Z. Wu and T. Zhang, *Angew. Chem., Int. Ed.*, 2023, **62**, e202304452.

80 C. Mao, L. Yu, J. Li, J. Zhao and L. Zhang, *Appl. Catal., B*, 2018, **224**, 612–620.

81 C. Mao, J. Wang, Y. Zou, Y. Shi, C. J. Viasus, J. Y. Y. Loh, M. Xia, S. Ji, M. Li, H. Shang, M. Ghoussoub, Y.-F. Xu, J. Ye, Z. Li, N. P. Kherani, L. Zheng, Y. Liu, L. Zhang and G. A. Ozin, *J. Am. Chem. Soc.*, 2023, **145**, 13134–13146.

82 C. Hu, X. Chen, J. Jin, Y. Han, S. Chen, H. Ju, J. Cai, Y. Qiu, C. Gao, C. Wang, Z. Qi, R. Long, L. Song, Z. Liu and Y. Xiong, *J. Am. Chem. Soc.*, 2019, **141**, 7807–7814.

83 J. Yuan, X. Yi, Y. Tang, M. Liu and C. Liu, *Adv. Funct. Mater.*, 2020, **30**, 1906983.

84 M. Vadai, D. K. Angell, F. Hayee, K. Sytwu and J. A. Dionne, *Nat. Commun.*, 2018, **9**, 4658.

85 L. Zhou, J. M. P. Martirez, J. Finzel, C. Zhang, D. F. Swearer, S. Tian, H. Robatjazi, M. Lou, L. Dong, L. Henderson, P. Christopher, E. A. Carter, P. Nordlander and N. J. Halas, *Nat. Energy*, 2020, **5**, 61–70.

86 Y. Yuan, L. Zhou, H. Robatjazi, J. L. Bao, J. Zhou, A. Bayles, L. Yuan, M. Lou, M. Lou, S. Khatiwada, E. A. Carter, P. Nordlander and N. J. Halas, *Science*, 2022, **378**, 889–893.